

The Origin of Magnetic Anisotropy and Single-molecule Magnet Behavior in Chromium(II)-based Extended Metal Atom Chains

Andrea Cornia,^{a} Anne-Laure Barra,^b Vladimir Bulicanu,^c Rodolphe Clérac,^c Miguel Cortijo,^c
Elizabeth A. Hillard,^{c*} Rita Galavotti,^a Alessandro Lunghi,^d Alessio Nicolini,^{a,e} Mathieu Rouzières,^c
Lorenzo Sorace^f and Federico Totti^{f*}*

^aDepartment of Chemical and Geological Sciences, University of Modena and Reggio Emilia & INSTM, 41125 Modena, Italy

^bLaboratoire National des Champs Magnétiques Intenses-CNRS, Université Grenoble-Alpes, 38042 Grenoble Cedex 9, France

^cUniv. Bordeaux, CNRS, Centre de Recherche Paul Pascal, UMR 5031, 33600 Pessac, France

^dSchool of Physics and CRANN Institute, Trinity College Dublin, Dublin 2, Ireland

^eDepartment of Physics, Informatics and Mathematics, University of Modena and Reggio Emilia, 41125 Modena, Italy

^fDepartment of Chemistry ‘Ugo Schiff’, University of Florence & INSTM, 50019 Sesto Fiorentino (FI), Italy

SUPPORTING INFORMATION

1. Synthesis

General. Unless otherwise noted, reagents and solvents were of commercial origin and used without further purification. Naphthalene was resublimed and NaSCN was recrystallized from acetone before use. Dichloromethane and diethyl ether for the synthesis of **1a**·Et₂O were purified using an Inert Technologies solvent purification system. For the synthesis of **2a**·4CHCl₃·2Et₂O and **2b** anhydrous dichloromethane (Sigma-Aldrich) was directly used, while chloroform was washed with water, stirred over CaCl₂ overnight and distilled under N₂; diethyl ether was pre-dried over CaCl₂ overnight and distilled from its sodium benzophenone ketyl solution under N₂; *n*-hexane was dried over 4A molecular sieves; all these solvents were degassed by three freeze-pump-thaw cycles.¹ The H₂tpda ligand was prepared as described elsewhere,^{2,3} recrystallized from boiling methanol or 2-propanol and checked by ¹H NMR spectroscopy and melting point measurement. All reactions involving chromium(II) complexes were carried out under Ar or N₂ atmosphere using Schlenk techniques or glovebox methods. Elemental analysis was carried out by Microlab Kolbe (Oberhausen, Germany, **1a**·Et₂O) or on a Carlo Erba EA1110 CHNS-O automatic analyzer (**2a**·4CHCl₃·2Et₂O and **2b**). The IR spectra were measured on a Nicolet 6700 FT-IR spectrometer using a Smart iTR accessory between 600 and 4000 cm⁻¹ with 4 cm⁻¹ resolution (**1a**·Et₂O) or on a JASCO 4700 FT-IR spectrometer between 400 and 4000 cm⁻¹ with 2 cm⁻¹ resolution (**2a**·4CHCl₃·2Et₂O and **2b**). Electrospray Ionization Mass Spectrometry (ESI-MS) was performed on an Agilent Technologies 6310A Ion Trap LC-MS(n) spectrometer.

Synthesis of [Cr₃(dpa)₄Cl₂]·Et₂O (1a**·Et₂O).** Complex **1a** was prepared following a literature procedure^{4,5} and isolated as the monodiethylether solvate^{6,7} by layering a dichloromethane solution with diethyl ether, yielding a crop of dark green crystals in 60% yield after a week of diffusion. Anal. Calcd for C_{43.7}H_{43.2}Cl_{2.2}Cr₃N₁₂O_{1.9} (**1a**·0.9Et₂O·0.1CH₂Cl₂·H₂O, 1000.87): C, 52.44; H, 4.35; N, 16.79. Found: C, 52.40; H, 4.19; N, 16.51. IR (ATR): $\tilde{\nu}_{\max}$ (cm⁻¹) 1603m, 1592s, 1546m, 1466m, 1457m, 1416s, 1369m, 1356m, 1310m, 1280w, 1153m, 1145m, 1103m, 1055w, 1011m, 917w, 882w, 857m, 767s, 752w, 741m, 701w, 690w, 644m. Unit cell parameters at 85 K were found consistent with those previously reported by Cotton, Murillo et al. at 213 K⁶ and by Overgaard, Iversen et al. at 100 K⁷ (see Table S1); structure solution and refinement confirmed that the crystalline material contains a minor fraction (~5-10%) of dichloromethane sharing the same crystallographic site with diethyl ether, as first noticed in Ref.⁷

Synthesis of [Cr₅(tpda)₄Cl₂]·4CHCl₃·2Et₂O (2a**·4CHCl₃·2Et₂O).** The compound was prepared in a glovebox starting from H₂tpda (0.448 mmol), CrCl₂ (0.672 mmol) and *t*BuOK (0.903 mmol) in refluxing naphthalene (2.0 g). We herein report the crystallization and sample collection procedures, which remain vague in the original paper by Peng et al..⁸ After treating the cooled-down reaction mixture with *n*-hexane (3 × 15 mL) to remove naphthalene, the resulting brown solid was extracted with dichloromethane (2 × 10 mL) yielding a dark-brown solution. The solvent was completely evaporated to give a bronze-colored solid, which was dissolved into the minimum amount of chloroform and the solution was filtered. Upon slow diffusion of diethyl ether vapors the compound crystallized as large, lustrous brown-black prisms that were easily separated from a tan powdery fraction by flotation in Et₂O:CHCl₃ 5:1 v/v (~30% yield). Their composition, IR spectra

and unit cell parameters (Table S1) were consistent with the compound first reported by Peng et al.⁸ Anal. Calcd for C₆₀H₄₄Cl₂Cr₅N₂₀ (**2a**, 1376.01): C, 52.37; H, 3.22; N, 20.36. Found (crystals kept at 0.15 torr for 8 hours): C, 52.22; H, 3.29; N, 19.61. ESI-MS (CH₂Cl₂ solution, direct infusion): *m/z* 1376.2 ([M]⁺, 100%). IR (crystals kept at 0.15 torr for 8 hours, KBr disk): $\tilde{\nu}_{\text{max}}$ (cm⁻¹) 1604m, 1578m, 1548m, 1474m, 1453m, 1422s, 1408s, 1348m, 1335m, 1300w, 1263w, 1155m, 1007w, 772m, 736w.

Synthesis of [Cr₅(tpda)₄(NCS)₂] (2b). To avoid use of water, the compound was prepared from **2a**·4CHCl₃·2Et₂O following the procedure described in Ref.⁹ rather than the original method in Ref.⁸ In a glovebox, **2a**·4CHCl₃·2Et₂O (49 mg, 0.024 mmol) was dissolved in CHCl₃ (3 mL) and treated with NaSCN (17.4 mg, 0.215 mmol) and additional CHCl₃ (9 mL). The mixture was stirred for three days to give a brown solution and a fine brown precipitate. The solvent was completely evaporated under reduced pressure and the solid extracted with CH₂Cl₂ (3 mL). A small fraction of the solution was evaporated to dryness and the solid residue checked by IR spectroscopy, which showed the expected C≡N stretching band of N-bound thiocyanate at 2035 cm⁻¹.⁸ Vapor diffusion of diethyl ether into the filtered extracts afforded brown-black prisms which were washed with Et₂O:CH₂Cl₂ 5:1 v/v (~30% yield). Their composition and unit cell parameters (Table S1) were consistent with the compound first reported by Peng et al.⁸ Anal. Calcd for C₆₂H₄₄Cr₅N₂₂S₂ (**2b**, 1421.27): C, 52.40; H, 3.12; N, 21.68; S, 4.51. Found (crystals kept at 0.2 torr for 6 hours): C, 52.75; H, 2.92; N, 21.54; S, 4.36. IR (crystals kept at 0.15 torr for 8 hours, ATR): $\tilde{\nu}_{\text{max}}$ (cm⁻¹) 2029m, 1602m, 1575m, 1545m, 1470m, 1451m, 1404s, 1333m, 1297w, 1258w, 1152m, 1007w, 764w, 731w.

2. Structural characterization

Table S1. Unit cell parameters obtained for known crystal phases investigated in this work.

compound	<i>T</i> (K)	<i>a</i> (Å)	<i>b</i> (Å)	<i>c</i> (Å)	α (°)	β (°)	γ (°)	<i>V</i> (Å ³)	Bravais lattice
1a ·Et ₂ O ^a	85	16.0384(5)	15.7660(5)	16.9975(5)	90	98.847(1)	90	4246.9(2)	<i>mP</i>
2a ·4CHCl ₃ ·2Et ₂ O ^b	298	28.51(2)	14.04(1)	25.08(2)	90	122.90(2)	90	8429(11)	<i>mC</i>
2b ^b	298	10.782(8)	10.782(8)	26.15(2)	90	90	90	3040(4)	<i>tI</i>

^a Bruker Quazar SMART APEXII diffractometer (Mo-K α radiation). ^b Bruker-Nonius X8APEX four-circle diffractometer (Mo-K α radiation).

Table S2. Crystal data and structure refinement for **1b**·0.4CH₂Cl₂.

Molecular formula	C _{42.40} H _{32.80} Cl _{0.80} Cr ₃ N ₁₄ S ₂	
Formula weight	986.90	
Temperature (K)	120(2)	
Wavelength (Å)	0.71073	
Crystal system	monoclinic	
Space group	<i>C</i> 2/ <i>c</i> (No. 15)	
Unit cell dimensions (Å, °)	<i>a</i> = 62.348(3),	α = 90
	<i>b</i> = 15.4922(7),	β = 106.305(2)
	<i>c</i> = 23.0405(11),	γ = 90
Unit cell volume (Å ³)	21360.1(17)	
<i>Z</i>	20	
Calculated density (Mg/m ³)	1.534	
Absorption coefficient (mm ⁻¹)	0.948	
<i>F</i> (000)	10056	
Crystal size (mm ³)	0.345 × 0.175 × 0.074	
Theta range for data collection (°)	1.664 to 25.423	
Index ranges	−70 ≤ <i>h</i> ≤ 75, −18 ≤ <i>k</i> ≤ 18, −27 ≤ <i>l</i> ≤ 27	
Reflections collected/independent	149744/19669 [<i>R</i> (int) = 0.1099]	
Completeness to theta = 25.423°	99.7%	
Absorption correction	semi-empirical from equivalents	
Max. and min. transmission	0.7452 and 0.6846	
Refinement method	Full-matrix least-squares on <i>F</i> ²	
Data / restraints / parameters	19669 / 3 / 1414	
Goodness-of-fit on <i>F</i> ²	1.025	
Final <i>R</i> indices [<i>I</i> > 2σ(<i>I</i>)]	<i>R</i> ₁ = 0.0634 ^a , <i>wR</i> ₂ = 0.1318 ^b	
<i>R</i> indices (all data)	<i>R</i> ₁ = 0.1180 ^a , <i>wR</i> ₂ = 0.1546 ^b	

^a $R_1 = \sum ||F_o| - |F_c|| / \sum |F_o|$. ^b $wR_2 = [\sum [w(F_o^2 - F_c^2)^2] / \sum [w(F_o^2)^2]]^{1/2}$, $w = 1 / \sigma^2(F_o^2) + (aP)^2 + bP$, where $P = [\max(0 \text{ or } F_o^2) + 2(F_c^2)] / 3$, $a = 0.0498$ and $b = 144.3774$.

Table S3. Continuous Shape Measures¹⁰ for terminal ions in chromium(II)-based EMACs with different nuclearity (*n*) and axial ligands (X).

compound	<i>n</i>	X	<i>T</i> (K)	vOC-5 ^{a,b}	SPY-5 ^{a,c}	Ref. ^d
1a ·Et ₂ O	3	Cl ⁻	213	1.136 (Cr1), 1.110 (Cr3)	0.459 (Cr1), 0.513 (Cr3)	6
1b ·0.4CH ₂ Cl ₂	3	SCN ⁻	120	0.328 (Cr1), 0.336 (Cr3), 0.318 (Cr4), 0.325 (Cr6), 0.289 (Cr7)	0.777 (Cr1), 0.628 (Cr3), 0.694 (Cr4), 0.699 (Cr6), 0.737 (Cr7)	this work
2a ·4CHCl ₃ ·2Et ₂ O	5	Cl ⁻	213	1.130 (Cr1)	0.303 (Cr1)	11
2b	5	SCN ⁻	RT	0.317 (Cr1)	0.674 (Cr1)	8

^a Deviation between real and ideal coordination polyhedron. ^b Vacant octahedron (Johnson square pyramid, J1). ^c Square pyramid. ^d From which atomic coordinates have been taken.

3. Magnetic characterization

Sample preparation. Samples for magnetic measurements were prepared with strict exclusion of dioxygen and moisture in a glovebox. Freshly-filtered polycrystalline samples of **1a**·Et₂O (15.11 mg) and **1b**·0.4CH₂Cl₂ (17.90 mg), unsolvated complex **2a** (6.44 mg, obtained by prolonged vacuum treatment of **2a**·4CHCl₃·2Et₂O) and vacuum-dried crystals of **2b** (6.0 mg) were covered with Paratone® oil (typically 10-20 mg) to avoid magnetic torqueing and introduced in a sealed polyethylene bag (3 × 0.5 × 0.02 cm; typically 24-32 mg). Solvated crystals of **2a**·4CHCl₃·2Et₂O, covered and restrained in a minimum amount of frozen mother liquor (17.23 mg) within a sealed straw, were also measured for comparison. No evaporation of the mother liquor was observed during the measurements. The mass of the sample was estimated at about 13.2 mg after the measurements and right after the mother liquor removal/evaporation (about 5 minutes) under Ar. It is worth noting that under the microscope the crystals looked perfectly shiny and crystalline immediately after removal of the mother liquor. Nevertheless, because residual solvent could easily alter the mass of the sample, the actual mass was accurately determined (11.35 mg) by comparing the high-temperature magnetic data with those of the dry compound. Prior to the experiments, the field-dependent magnetization was measured at 100 K on each sample to exclude the presence of bulk ferromagnetic impurities.

Spin Hamiltonian calculations. Spin Hamiltonian calculations were carried out using in-house developed software in FORTRAN language based on F02ABF and E04FCF NAG routines for matrix diagonalization and least-square fitting, respectively.¹² The zero-field splitting *plus* Zeeman Hamiltonian in Eq. (1) was used to fit isothermal magnetization vs. field data using isotropic *g*, *D* and, occasionally, a preferential orientation coefficient *a*₂ and/or a scale factor as adjustable parameters. Preferential orientation effects were modelled with an axial probability function¹³ expressed as a linear combination of Legendre polynomials of even order, including only $P_0(\cos\theta) = 1$ and $P_2(\cos\theta) = (3\cos^2\theta - 1)/2$. The value of *a*₀ is fixed by the normalization condition, while a positive/negative value of *a*₂ indicates a prolate/oblate distribution of the easy axes, respectively, *i.e.* the "parallel" arrangement is more/less populated than in a randomly-oriented sample. The need for introducing preferential orientation was already encountered in the past in our

laboratories and shown to arise from a non statistical distribution of crystal orientations in samples comprising a small number of large crystals, and not from field-induced torquing. The estimated standard deviations of best-fit parameters, quoted in Tables 2 and S4, were calculated from the variances of the regression coefficients, as provided by routine E04YCF.¹²

Table S4. Magnetic parameters of chromium(II)-based EMACs with different nuclearity (n) and axial ligands (X), as determined by dc magnetic measurements (isothermal magnetization vs. field).

compound	n	X	S	g	D (cm ⁻¹)	a_2	scale factor
1a ·Et ₂ O	3	Cl ⁻	2 ^a	1.957(2)	-1.656(16)	0.067(2)	1.000 ^a
1b ·0.4CH ₂ Cl ₂	3	SCN ⁻	2 ^a	2.0360(17)	-1.711(12)	-0.0312(15)	1.000 ^a
2a ·4CHCl ₃ ·2Et ₂ O	5	Cl ⁻	2 ^a	1.9774(3)	-1.507(2)	-0.1501(3)	1.000 ^a
2a	5	Cl ⁻	2 ^a	1.9731(8)	-1.510(6)	0.000 ^a	1.000 ^a
2b	5	SCN ⁻	2 ^a	1.985 ^a	-1.696(4)	0.0889(4)	0.9247(3)

^aParameter held fixed.

3.1 Magnetic data for $[\text{Cr}_3(\text{dpa})_4\text{Cl}_2]\cdot\text{Et}_2\text{O}$ (**1a** $\cdot\text{Et}_2\text{O}$)

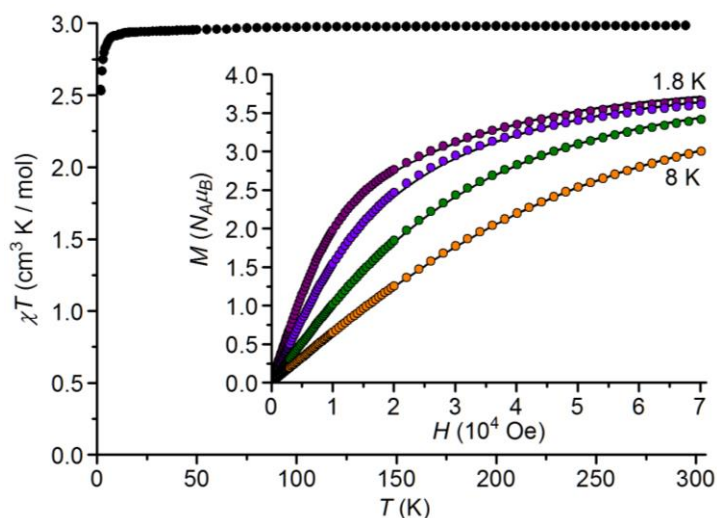


Figure S1. χT vs. T plot for **1a** $\cdot\text{Et}_2\text{O}$ in the temperature range 1.85-295 K at 1 kOe. At room temperature, the χT product is $2.98 \text{ cm}^3 \text{ K mol}^{-1}$. When the temperature is lowered, the χT product decreases reaching $2.54 \text{ cm}^3 \text{ K mol}^{-1}$ at 1.85 K. The inset presents M vs. H data measured at four different temperatures (1.8, 3.0, 5.0 and 8.0 K), along with the best-fit curves to the 452 data points with the parameters reported in the text.

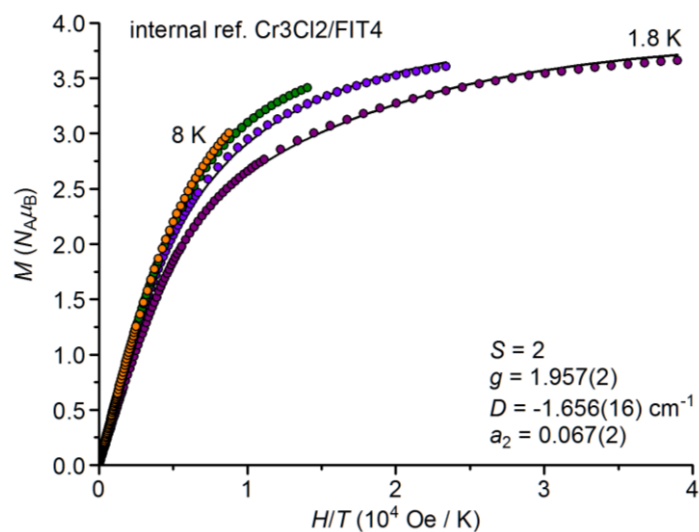


Figure S2. M vs. H/T plot for **1a** $\cdot\text{Et}_2\text{O}$ at four different temperatures (1.8, 3.0, 5.0 and 8.0 K), along with the best-fit curves to the 452 data points with the parameters reported in the text.

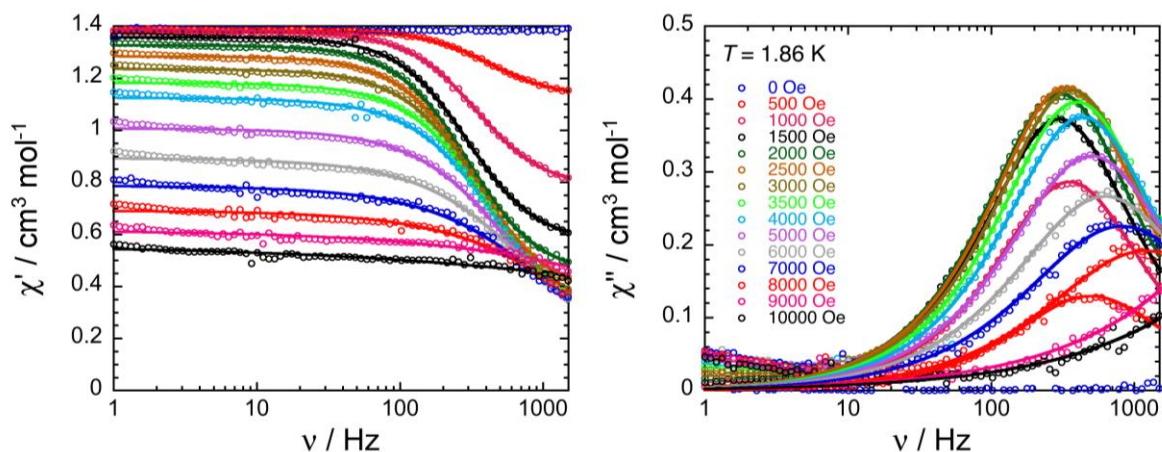


Figure S3. In-phase (left) and out-of-phase (right) components of the molar ac magnetic susceptibility of **1a**·Et₂O measured at 1.86 K as a function of applied dc field between 0 and 10 kOe. The solid curves on the figures provide the best fit using the generalized Debye model.

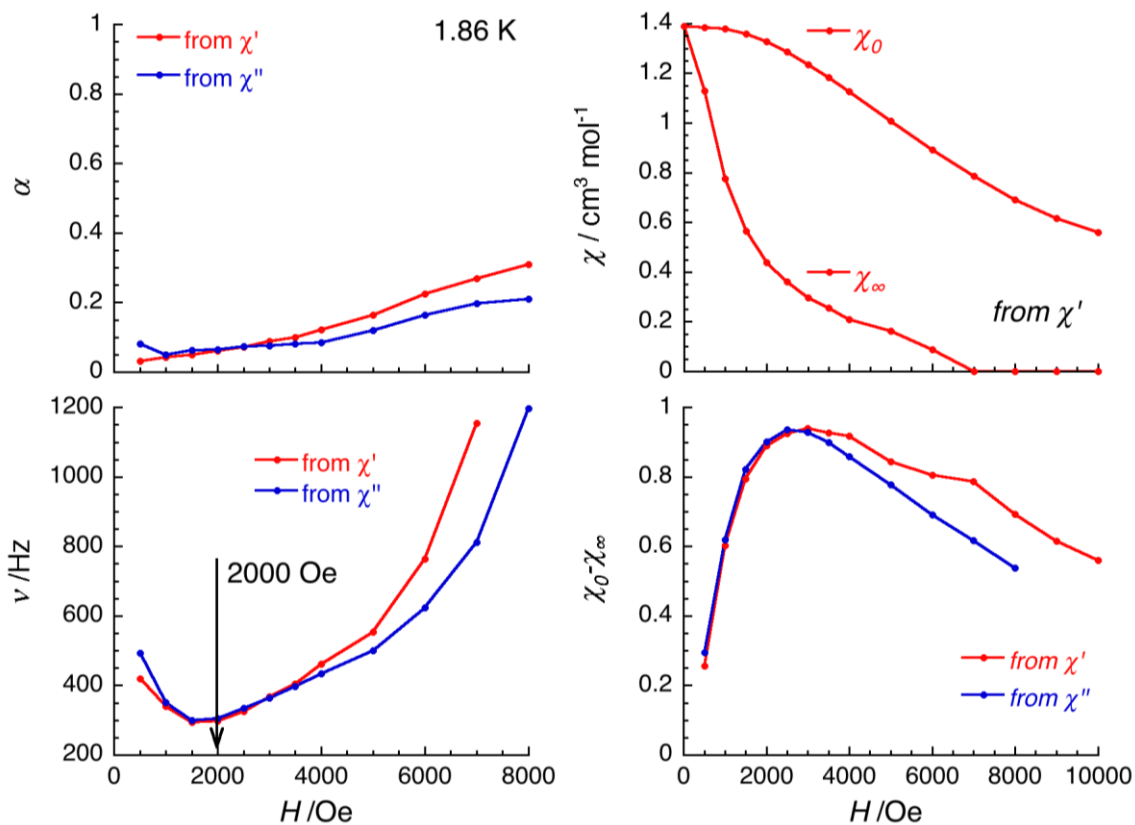


Figure S4. Field dependence of the parameters α , ν , χ_0 , χ_∞ and $\chi_0 - \chi_\infty$ between 0 and 10 kOe deduced from the generalized Debye fit of the frequency dependence of the real (χ') and imaginary (χ'') components of the ac susceptibility at 1.86 K, shown in Figure S3, for **1a**·Et₂O. The slowest relaxation occurs at 2.0 kOe.

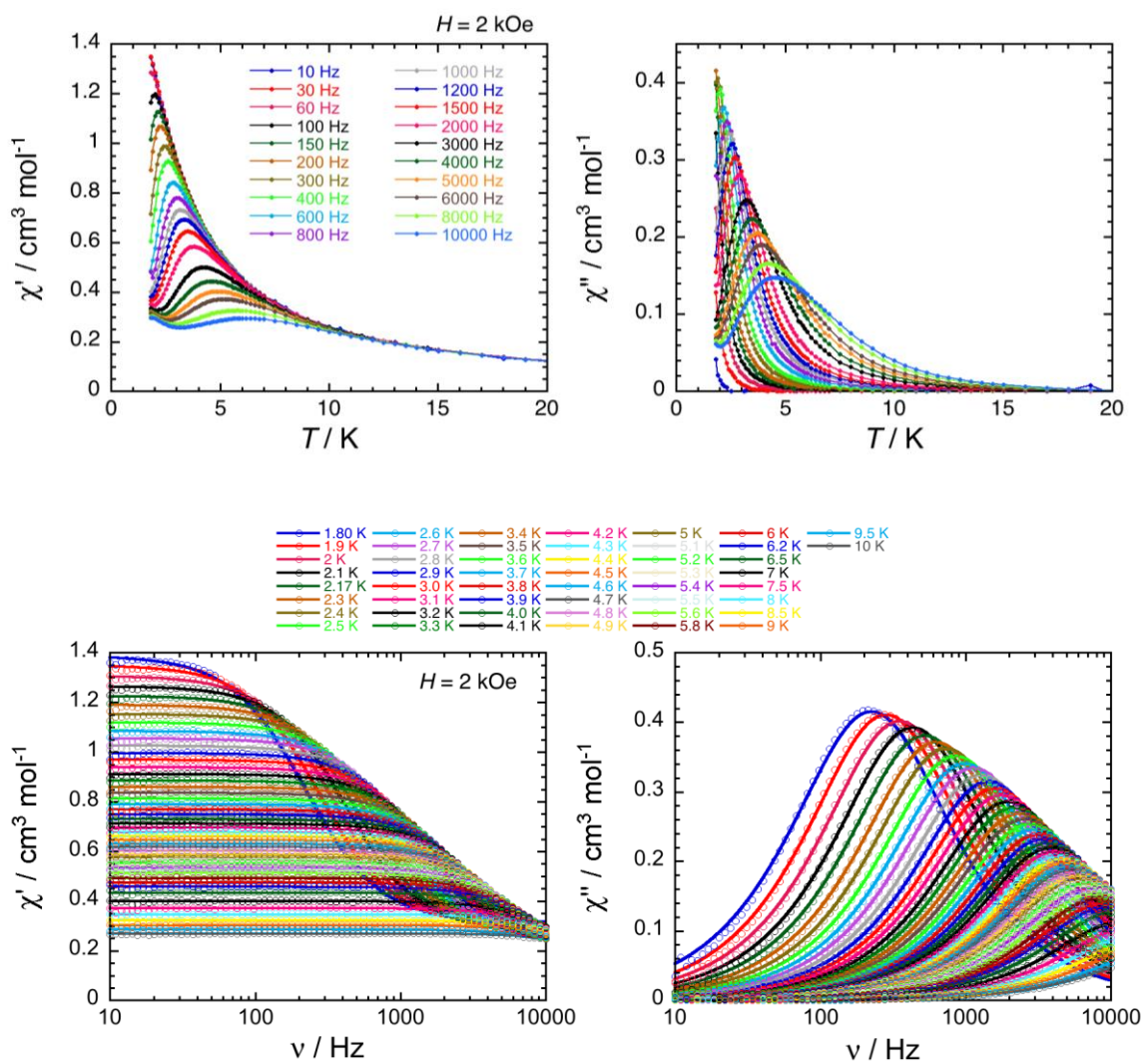


Figure S5. In-phase (left) and out-of-phase (right) components of the molar ac magnetic susceptibility of **1a**·Et₂O measured as a function of temperature at different frequencies (top) and as a function of frequency at different temperatures (bottom) at 2.0 kOe. While solid lines on the top figures are visual guides, the solid curves on the bottom figures provide the best fit using the generalized Debye model.

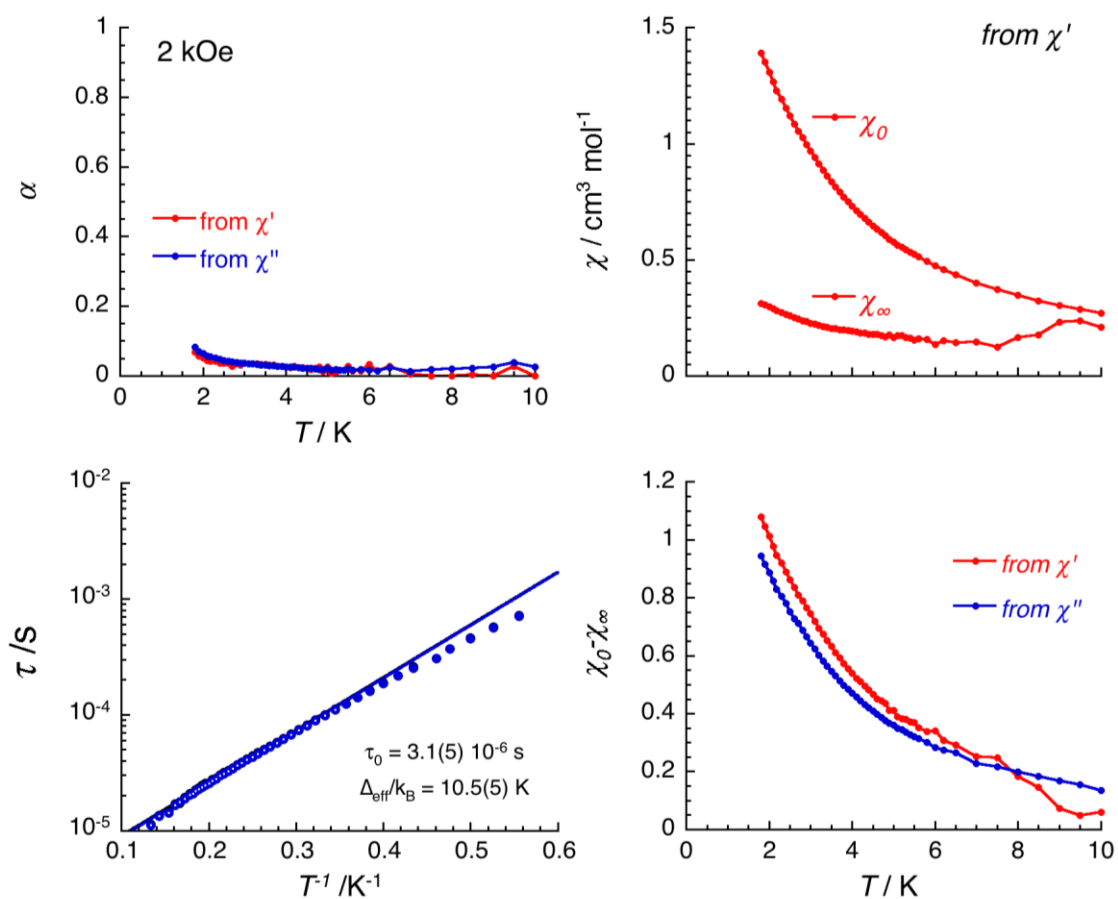


Figure S6. Temperature dependence of the parameters α , τ , χ_0 , χ_∞ and $\chi_0 - \chi_\infty$ between 1.8 and 10 K deduced from the generalized Debye fit of the frequency dependence of the real (χ') and imaginary (χ'') components of the ac susceptibility at 2.0 kOe, shown in Figure S5, for **1a**·Et₂O. On the bottom left figure, the temperature dependence of the relaxation time of **1a**·Et₂O at 2.0 kOe between 1.8 and 7.5 K (treatment of χ' vs. ν and χ'' vs. ν curves gives indistinguishable results; both sets of data are plotted). The solid line provides the best fit Arrhenius law to the data represented with hollow points with the reported parameter set.

3.2 Magnetic data for $[\text{Cr}_3(\text{dpa})_4(\text{NCS})_2] \cdot 0.4\text{CH}_2\text{Cl}_2$ (**1b**·0.4CH₂Cl₂)

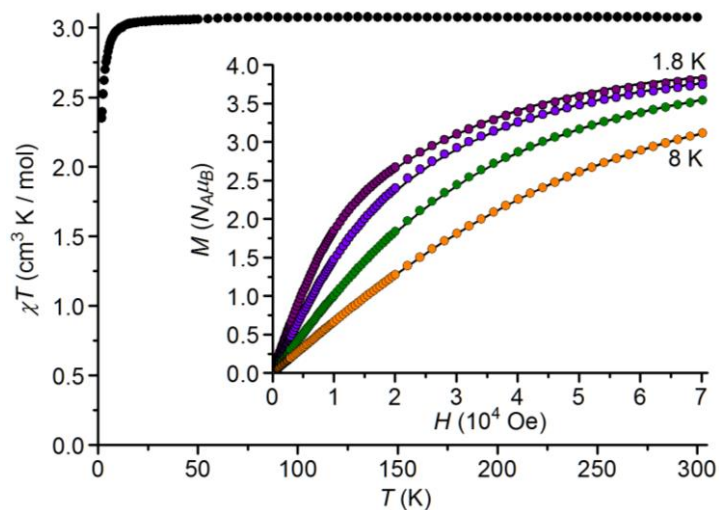


Figure S7. χT vs. T plot for **1b**·0.4CH₂Cl₂ in the temperature range 1.85–300 K at 1 kOe. At room temperature, the χT product is 3.08 cm³ K mol⁻¹. When the temperature is lowered, the χT product decreases reaching 2.35 cm³ K mol⁻¹ at 1.85 K. The inset presents M vs. H data measured at four different temperatures (1.8, 3.0, 5.0 and 8.0 K), along with the best-fit curves to the 452 data points with the parameters reported in the text.

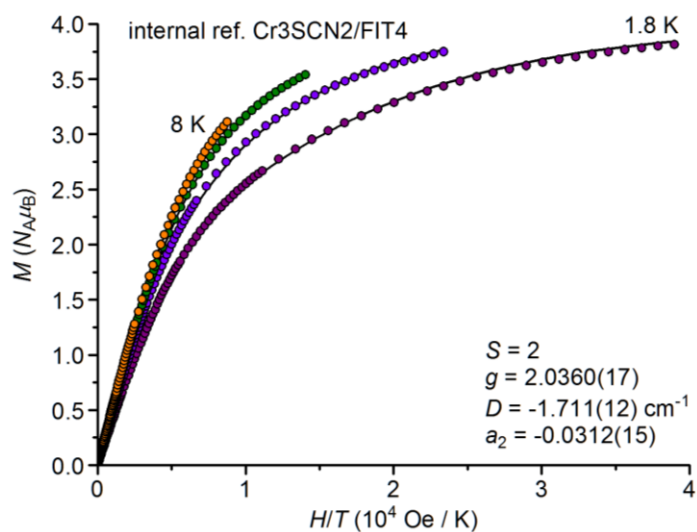


Figure S8. M vs. H/T plot for **1b**·0.4CH₂Cl₂ at four different temperatures (1.8, 3.0, 5.0 and 8.0 K), along with the best-fit curves to the 452 data points with the parameters reported in the text.

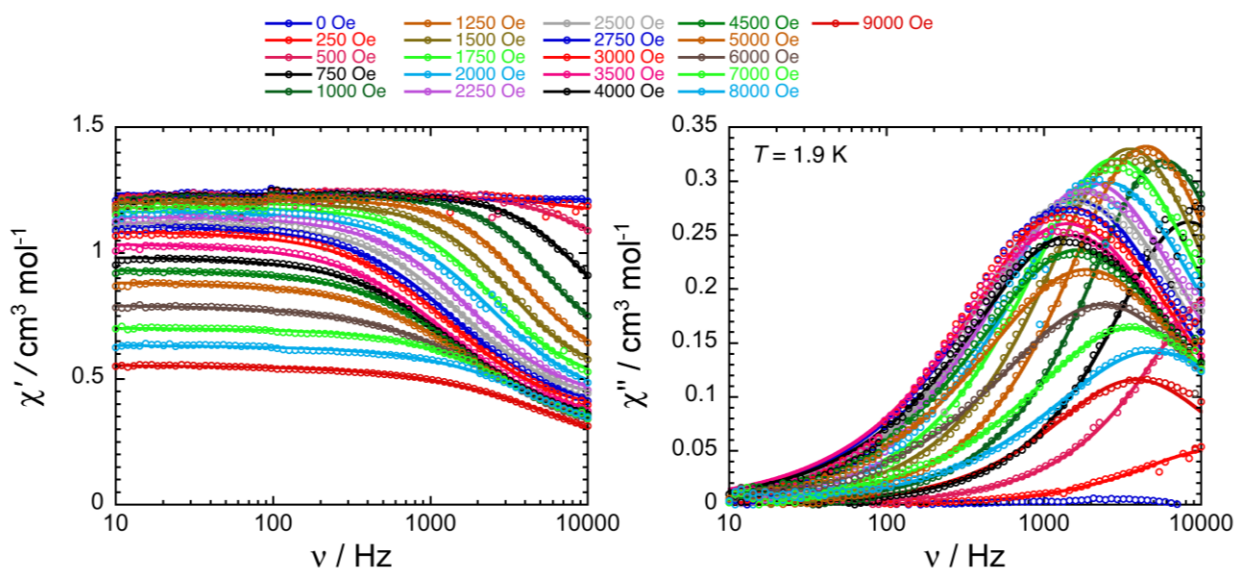


Figure S9. In-phase (left) and out-of-phase (right) components of the molar ac magnetic susceptibility of **1b**·0.4CH₂Cl₂ measured at 1.9 K as a function of applied dc field between 0 and 9 kOe. The solid curves on the figures provide the best fit using the generalized Debye model.

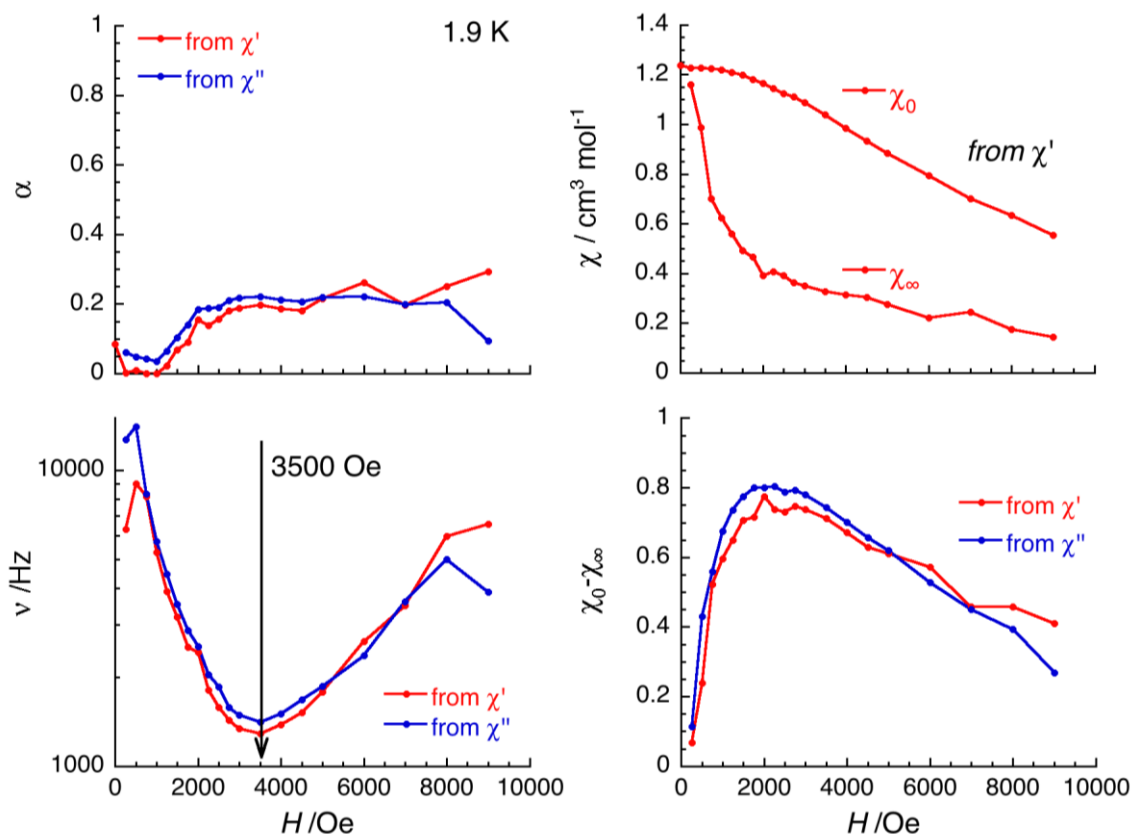


Figure S10. Field dependence of the parameters α , ν , χ_0 , χ_∞ and $\chi_0 - \chi_\infty$ between 0 and 9 kOe deduced from the generalized Debye fit of the frequency dependence of the real (χ') and imaginary (χ'') components of the ac susceptibility at 1.9 K, shown in Figure S9, for **1b**·0.4CH₂Cl₂. The slowest relaxation occurs at 3.5 kOe.

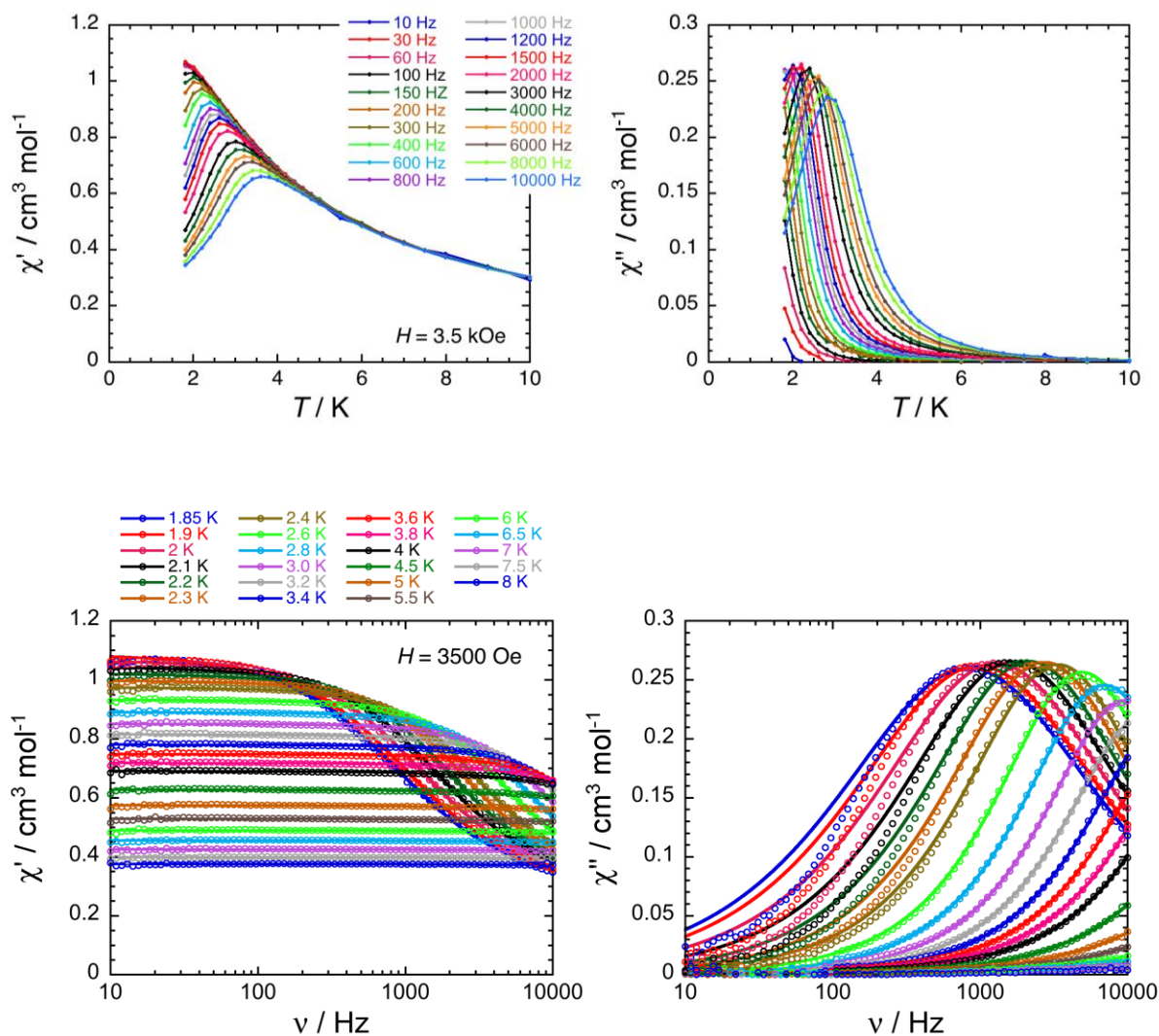


Figure S11. In-phase (left) and out-of-phase (right) components of the molar ac magnetic susceptibility of $\mathbf{1b} \cdot 0.4\text{CH}_2\text{Cl}_2$ measured as a function of temperature at different frequencies (top) and as a function of frequency at different temperatures (bottom) at 3.5 kOe. While solid lines on the top figures are visual guides, the solid curves on the bottom figures provide the best fit using the generalized Debye model.

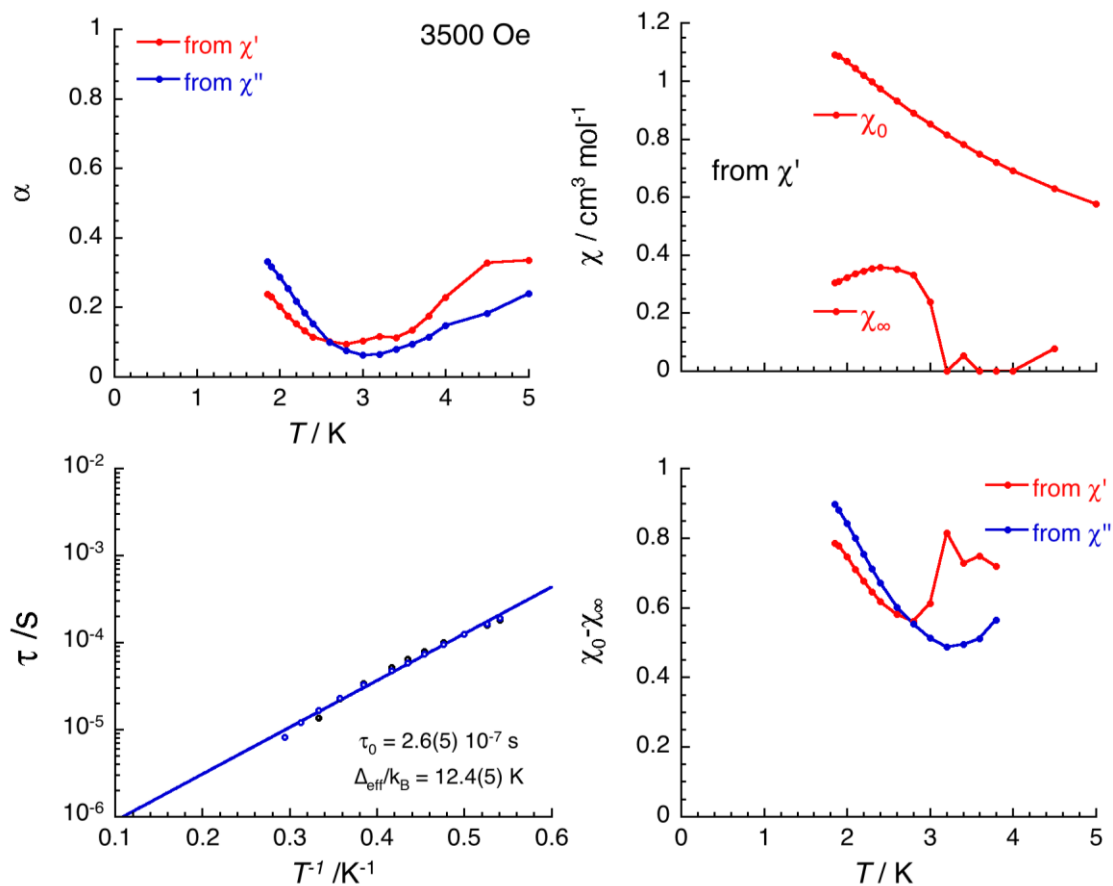


Figure S12. Temperature dependence of the parameters α , τ , χ_0 , χ_∞ and $\chi_0 - \chi_\infty$ between 1.85 and 5 K deduced from the generalized Debye fit of the frequency dependence of the real (χ') and imaginary (χ'') components of the ac susceptibility at 3.5 kOe, shown in Figure S11, for **1b**·0.4CH₂Cl₂. On the bottom left figure, the temperature dependence of the relaxation time of **1b**·0.4CH₂Cl₂ at 3.5 kOe between 1.85 and 3.4 K (treatment of χ' vs. ν and χ'' vs. ν curves gives indistinguishable results; both sets of data are plotted). The solid line provides the best fit Arrhenius law to the data represented with hollow points with the reported parameter set.

3.3 Magnetic data for $[\text{Cr}_5(\text{tdpa})_4\text{Cl}_2]$ (**2a**)

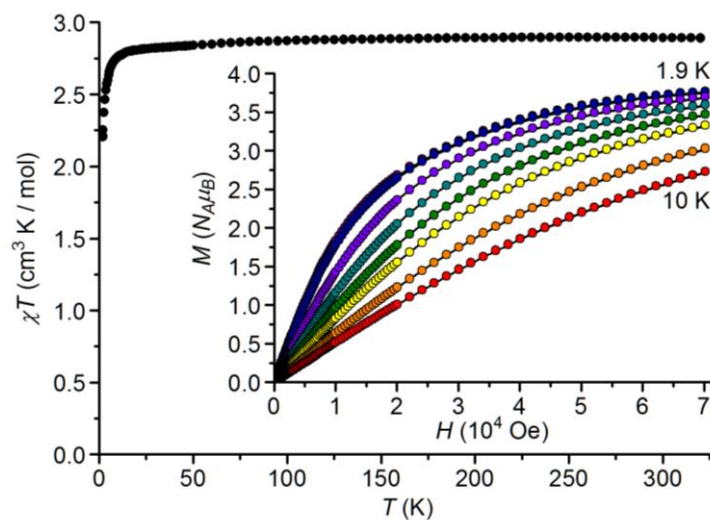


Figure S13. χT vs. T plot for **2a** at 1 kOe in the temperature range 1.85-320 K. At room temperature, the χT product is $2.89 \text{ cm}^3 \text{ K mol}^{-1}$. When the temperature is lowered, the χT product at 1 kOe decreases reaching $2.21 \text{ cm}^3 \text{ K mol}^{-1}$ at 1.85 K. The inset presents M vs. H data measured at eight different temperatures (1.9, 2.0, 3.0, 4.0, 5.0, 6.0, 8.0 and 10.0 K), along with the best-fit curves to the 904 data points with the parameters reported in the text.

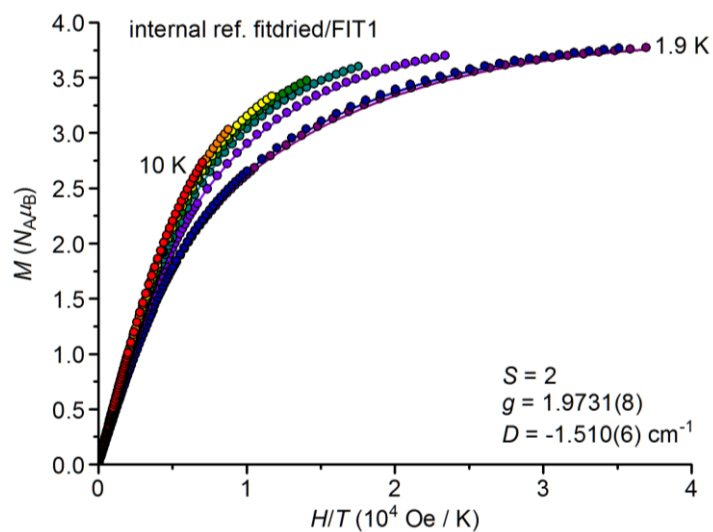


Figure S14. M vs. H/T plot for **2a** at temperatures between 1.9 and 10.0 K. The solid curves provide the best fit to the 904 data points with the reported set of parameters.

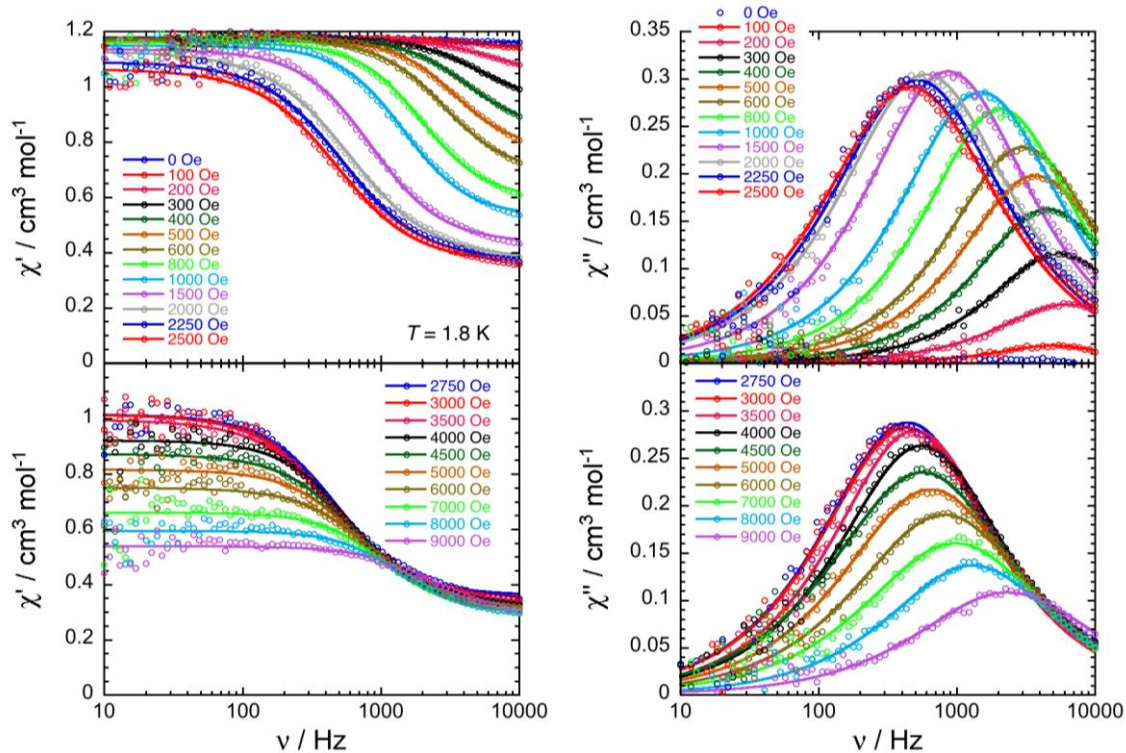


Figure S15. In-phase (left) and out-of-phase (right) components of the molar ac magnetic susceptibility of **2a** measured at 1.8 K as a function of applied dc field between 0 and 9 kOe. The solid curves on the figures provide the best fit using the generalized Debye model.

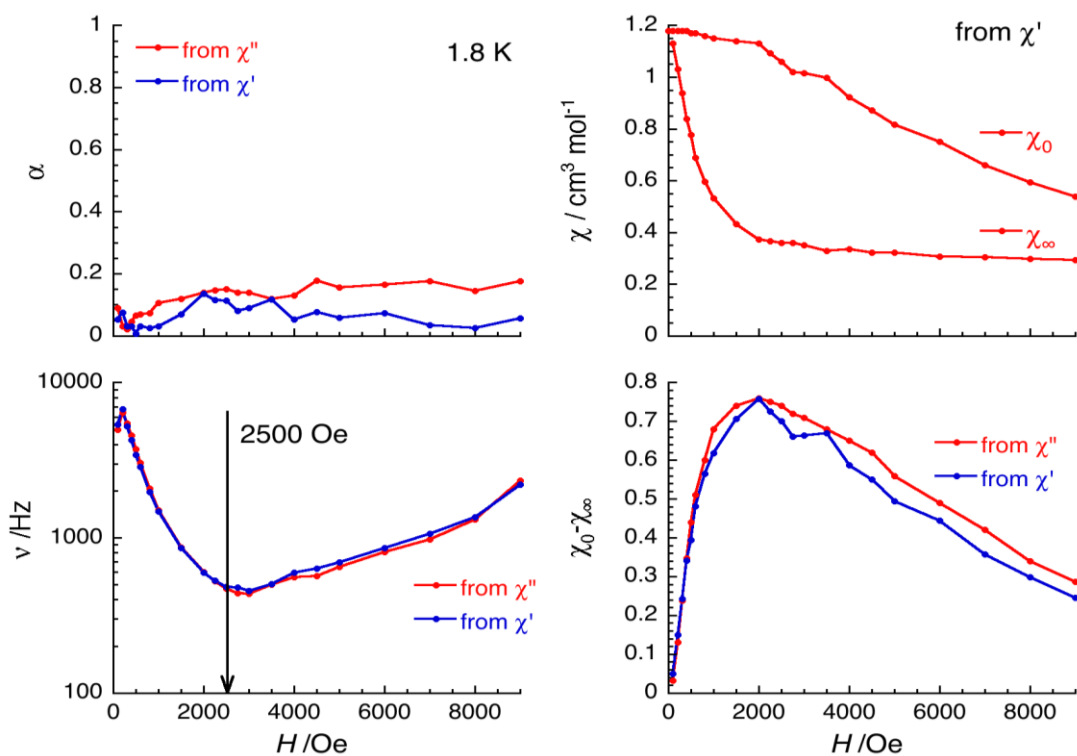


Figure S16. Field dependence of the parameters α , ν , χ_0 , χ_∞ and $\chi_0 - \chi_\infty$ between 0 and 9 kOe deduced from the generalized Debye fit of the frequency dependence of the real (χ') and imaginary (χ'') components of the ac susceptibility at 1.8 K, shown in Figure S15, for **2a**. The slowest relaxation occurs at 2.5 kOe.

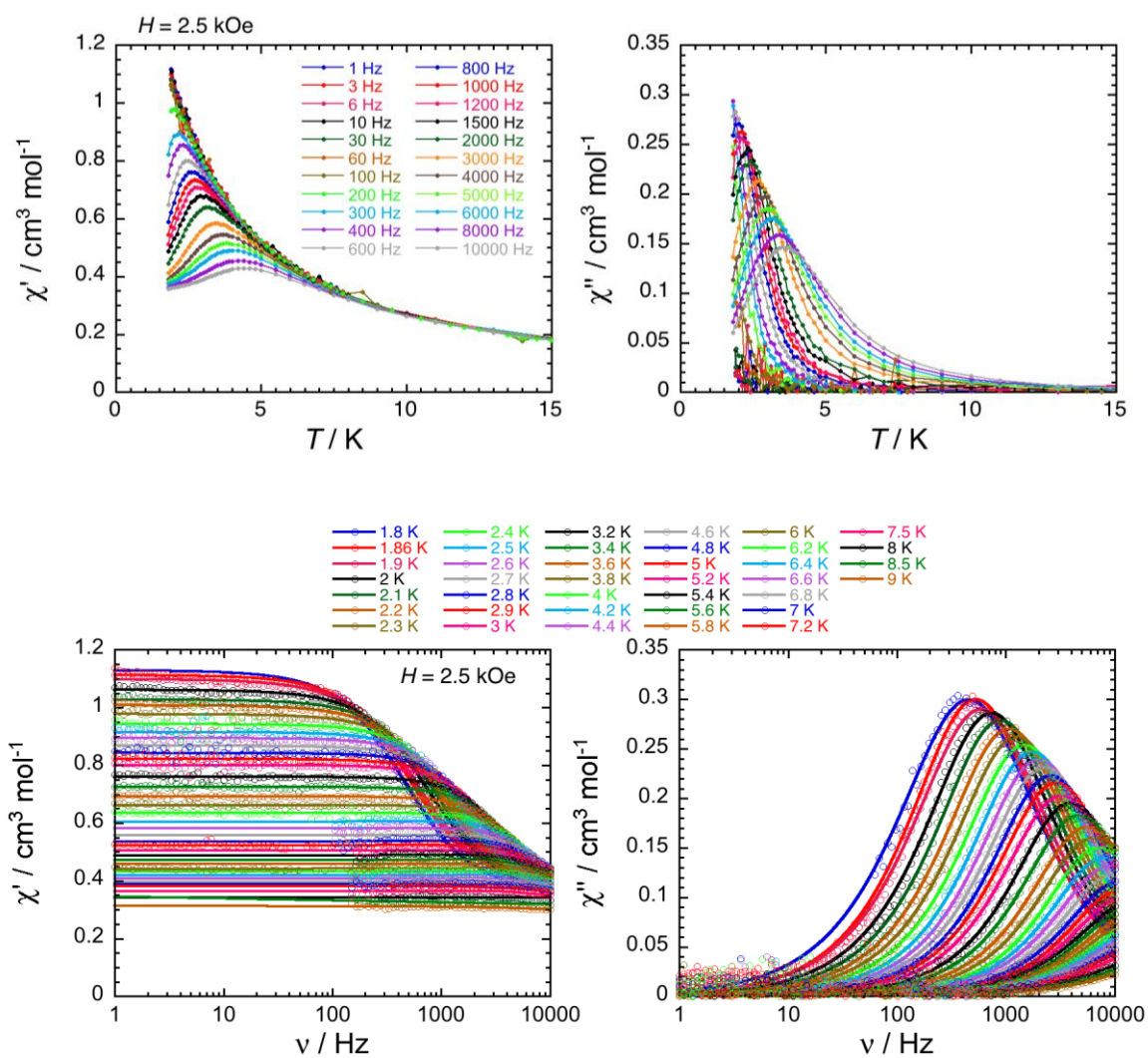


Figure S17. In-phase (left) and out-of-phase (right) components of the molar ac magnetic susceptibility of **2a** measured as a function of temperature at different frequencies (top) and as a function of frequency at different temperatures (bottom) at 2.5 kOe. While solid lines on the top figures are visual guides, the solid curves on the bottom figures provide the best fit using the generalized Debye model.

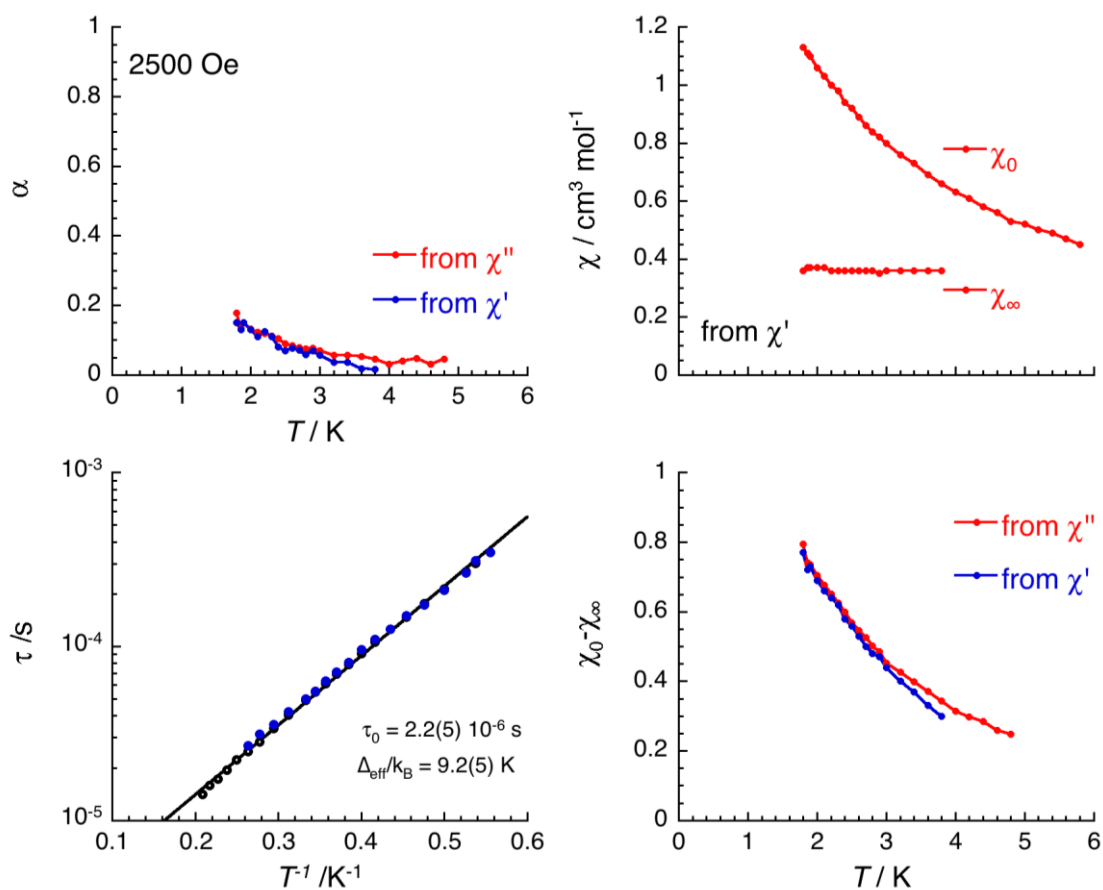


Figure S18. Temperature dependence of the parameters α , τ , χ_0 , χ_∞ and $\chi_0 - \chi_\infty$ between 1.8 and 6 K deduced from the generalized Debye fit of the frequency dependence of the real (χ') and imaginary (χ'') components of the ac susceptibility at 2.5 kOe, shown in Figure S17, for **2a**. On the bottom left figure, the temperature dependence of the relaxation time of **2a** at 2.5 kOe between 1.8 and 4.8 K (treatment of χ' vs. ν and χ'' vs. ν curves gives indistinguishable results; both sets of data are plotted). The solid line provides the best fit Arrhenius law to the data with the reported parameter set.

3.4 Magnetic data for $[\text{Cr}_5(\text{tdpa})_4\text{Cl}_2]\cdot 4\text{CHCl}_3\cdot 2\text{Et}_2\text{O}$ (**2a**· $4\text{CHCl}_3\cdot 2\text{Et}_2\text{O}$)

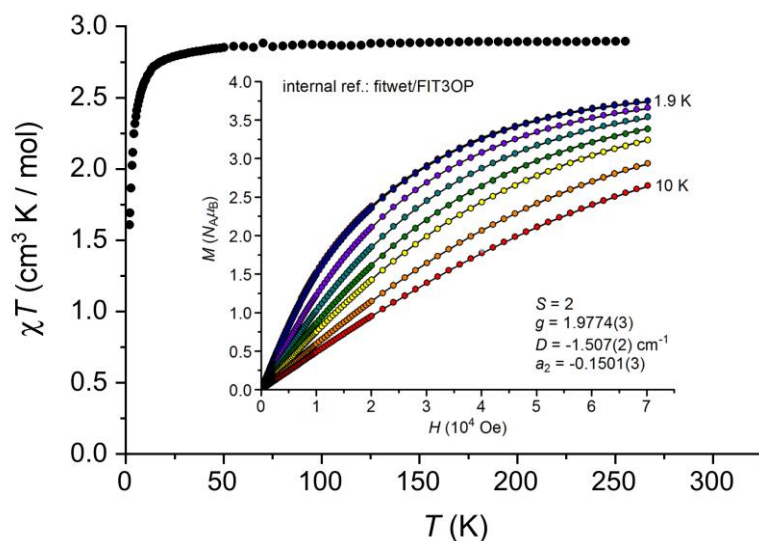


Figure S19. χT vs. T plot for **2a**· $4\text{CHCl}_3\cdot 2\text{Et}_2\text{O}$ in the temperature range 1.86–255 K at 1 kOe. At the highest temperatures reached (255 K to avoid in-situ solvent loss), the χT product is $2.89 \text{ cm}^3 \text{ K mol}^{-1}$. When the temperature is lowered, the χT product at 1 kOe decreases reaching $1.61 \text{ cm}^3 \text{ K mol}^{-1}$ at 1.86 K. The inset presents M vs. H plot for **2a**· $4\text{CHCl}_3\cdot 2\text{Et}_2\text{O}$ at eight temperature values between 1.9 and 10.0 K (1.9, 2.0, 3.0, 4.0, 5.0, 6.0, 8.0, 10.0 K). The solid curves provide the best fit to the 912 experimental data points with the reported set of parameters. The highest magnetization value detected is $3.75 N_A \mu_B$ at 1.9 K and 70 kOe.

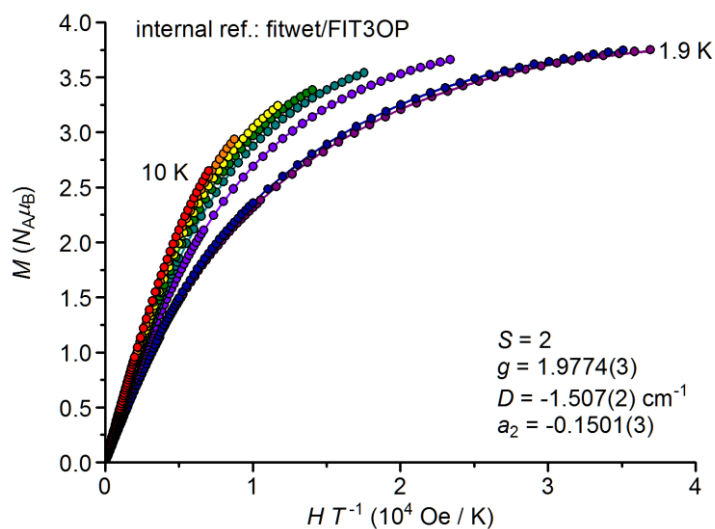


Figure S20. M vs. H/T plot for **2a**· $4\text{CHCl}_3\cdot 2\text{Et}_2\text{O}$ at temperatures between 1.9 and 10.0 K (1.9, 2.0, 3.0, 4.0, 5.0, 6.0, 8.0, 10.0 K). The solid curves provide the best fit to the 912 experimental data points with the reported set of parameters.

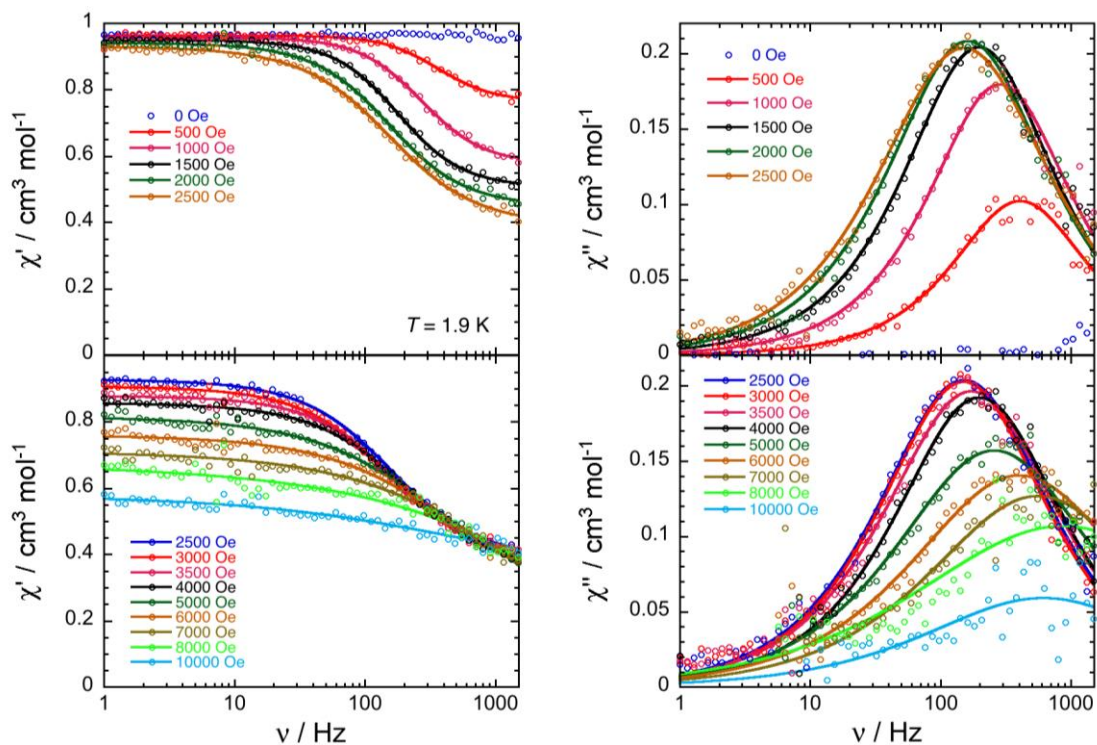


Figure S21. In-phase (left) and out-of-phase (right) components of the molar ac magnetic susceptibility of **2a**·4CHCl₃·2Et₂O measured at 1.9 K as a function of applied dc field between 0 and 10 kOe. The solid curves on the figures provide the best fit using the generalized Debye model.

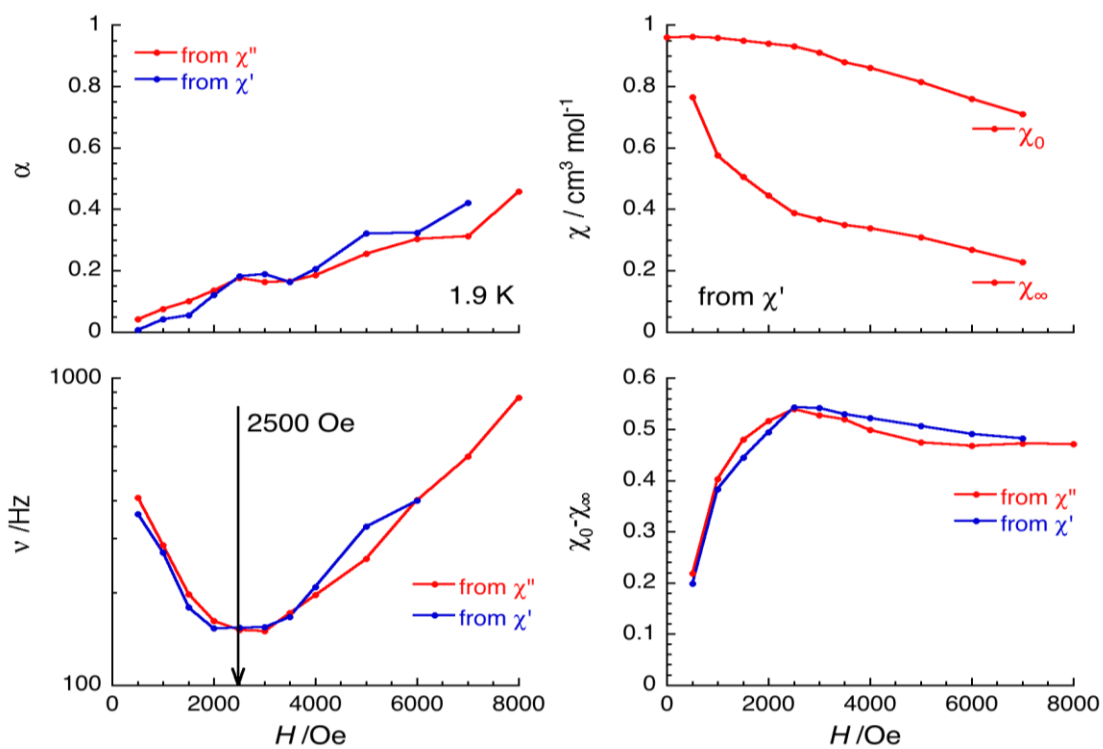


Figure S22. Field dependence of the parameters α , ν , χ_0 , χ_∞ and $\chi_0 - \chi_\infty$ between 0 and 8 kOe deduced from the generalized Debye fit of the frequency dependence of the real (χ') and imaginary (χ'') components of the ac susceptibility at 1.9 K, shown in Figure S21, for **2a**·4CHCl₃·2Et₂O. The slowest relaxation occurs at 2.5 kOe.

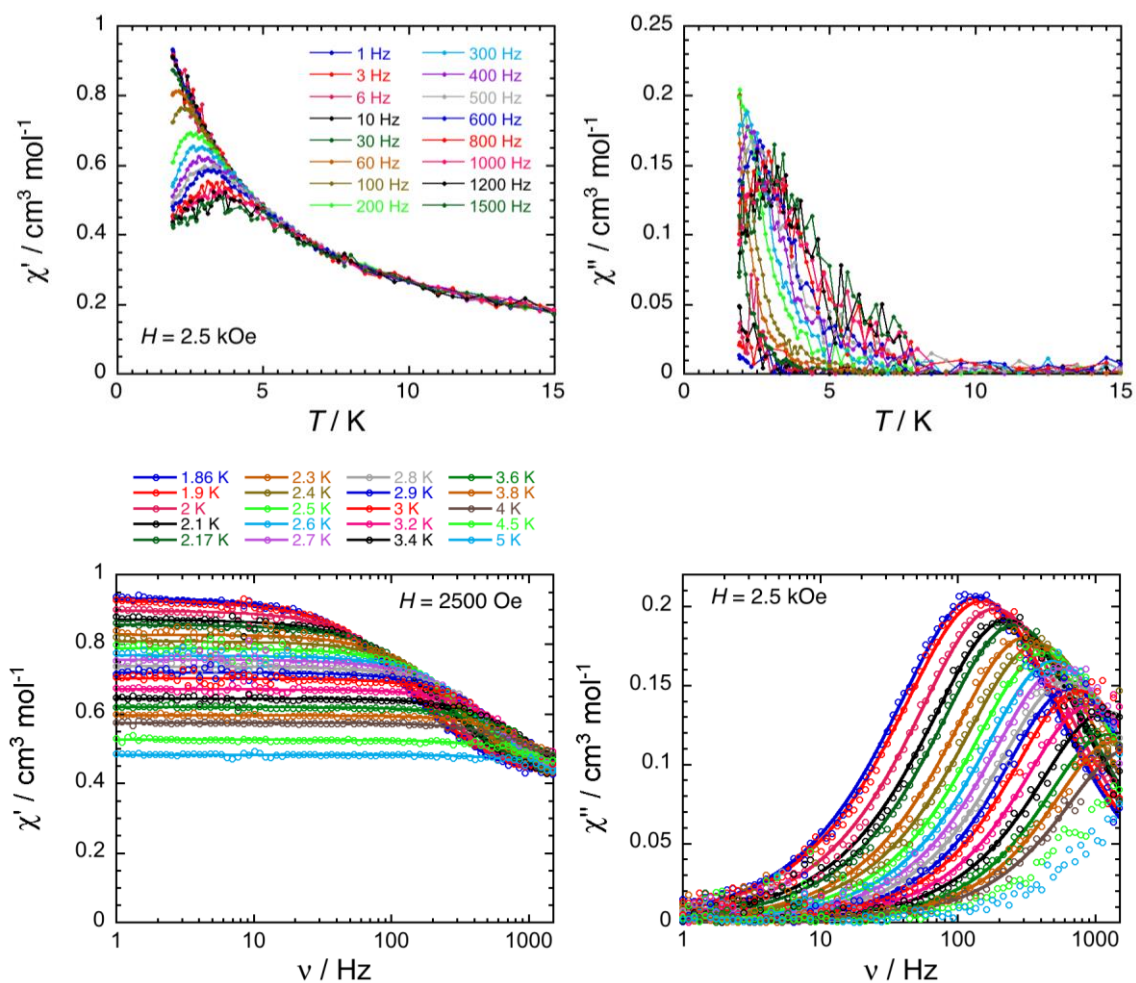


Figure S23. In-phase (left) and out-of-phase (right) components of the molar ac magnetic susceptibility of $2a \cdot 4\text{CHCl}_3 \cdot 2\text{Et}_2\text{O}$ measured as a function of temperature at different frequencies (top) and as a function of frequency at different temperatures (bottom) at 2.5 kOe. While solid lines on the top figures are visual guides, the solid curves on the bottom figures provide the best fit using the generalized Debye model.

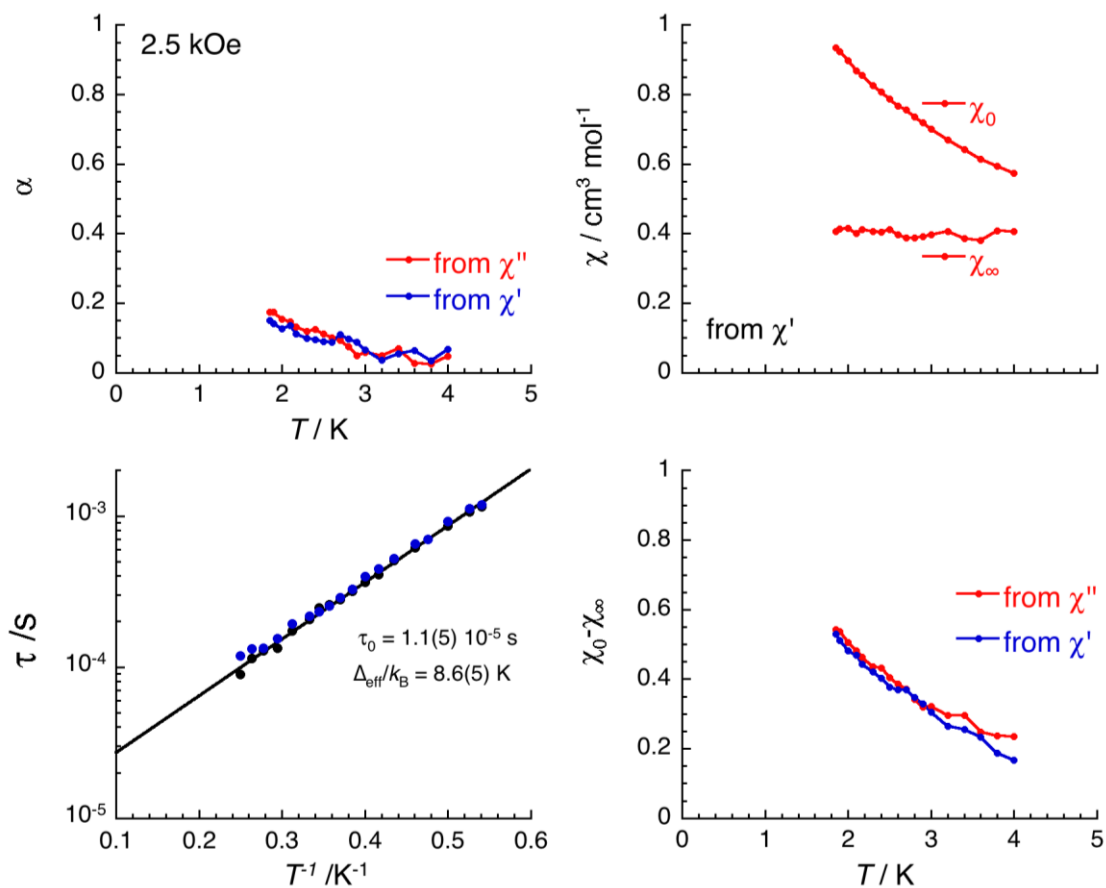


Figure S24. Temperature dependence of the parameters α , τ , χ_0 , χ_∞ and $\chi_0 - \chi_\infty$ between 1.86 and 4 K deduced from the generalized Debye fit of the frequency dependence of the real (χ') and imaginary (χ'') components of the ac susceptibility at 2.5 kOe, shown in Figure S23, for $2\mathbf{a} \cdot 4\text{CHCl}_3 \cdot 2\text{Et}_2\text{O}$. On the bottom left figure, the temperature dependence of the relaxation time of $2\mathbf{a} \cdot 4\text{CHCl}_3 \cdot 2\text{Et}_2\text{O}$ at 2.5 kOe between 1.86 and 4 K (treatment of χ' vs. ν and χ'' vs. ν curves gives indistinguishable results; both sets of data are plotted). The solid line provides the best fit Arrhenius law with the reported parameter set.

3.5 Magnetic data for $[\text{Cr}_5(\text{tpda})_4(\text{NCS})_2]$ (**2b**)

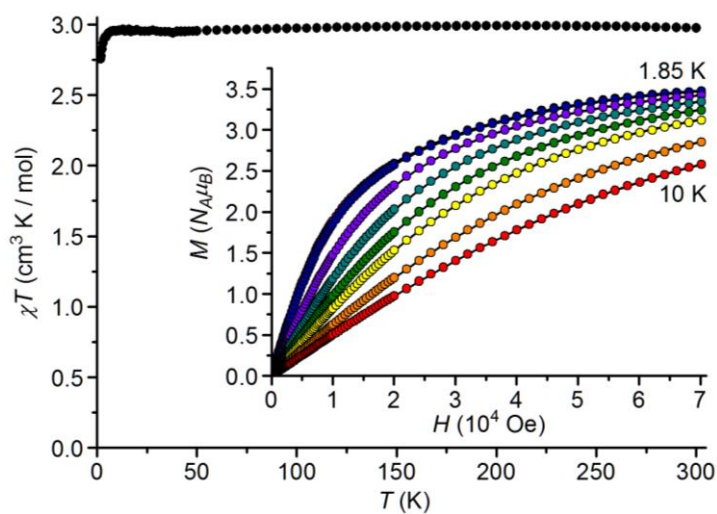


Figure S25. χT vs. T plot for **2b** in the temperature range 1.85–300 K at 1 kOe. At room temperature, the χT product is $2.96 \text{ cm}^3 \text{ K mol}^{-1}$. When the temperature is lowered, the χT product at 1 kOe decreases reaching $2.75 \text{ cm}^3 \text{ K mol}^{-1}$ at 1.85 K. The inset presents M vs. H data measured at eight different temperatures (1.85, 2.0, 3.0, 4.0, 5.0, 6.0, 8.0 and 10.0 K), along with the best-fit curves to the 900 data points with the parameters reported in the text. The highest magnetization value detected is $3.47 N_A \mu_B$ at 1.85 K and 70 kOe.

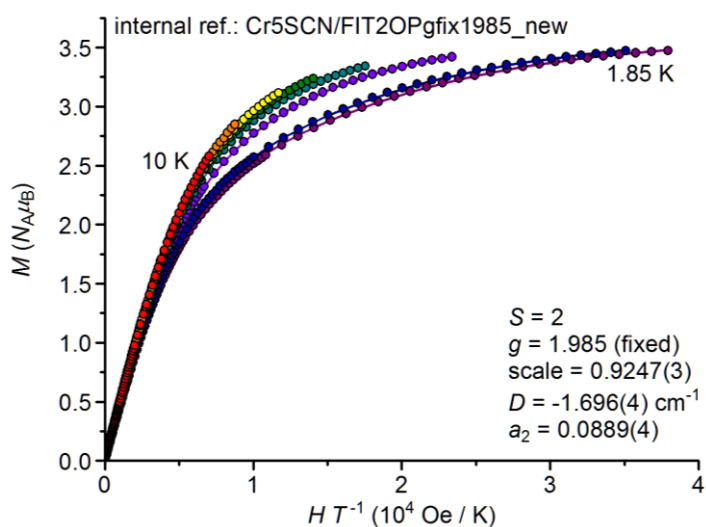


Figure S26. M vs. H/T plot for **2b** at temperatures between 1.85 and 10.0 K. The solid curves provide the best fit to the 900 data points with the reported set of parameters.

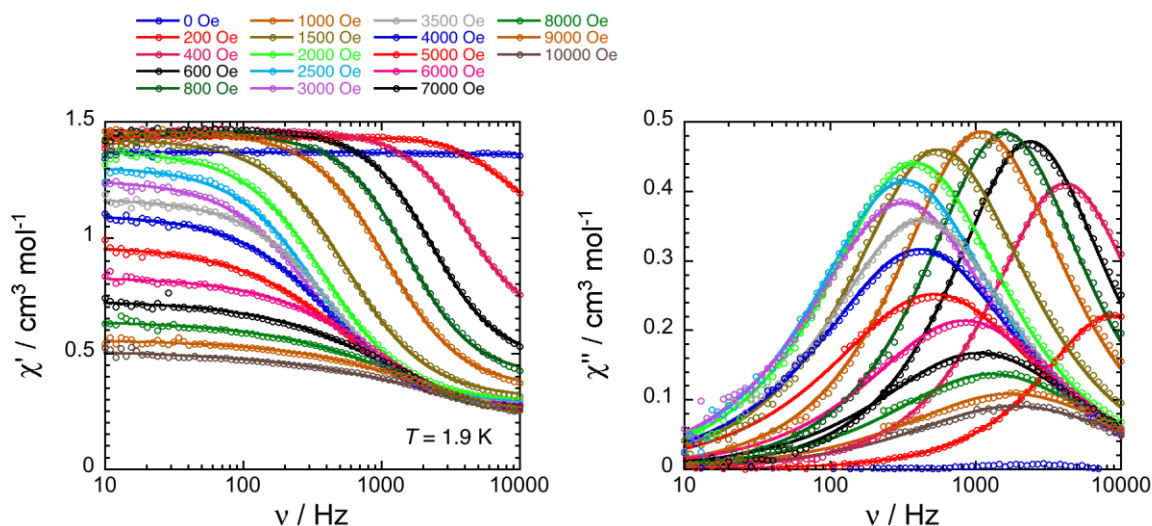


Figure S27. In-phase (left) and out-of-phase (right) components of the molar ac magnetic susceptibility of **2b** measured at 1.9 K as a function of applied dc field between 0 and 10 kOe. The solid curves on the figures provide the best fit using the generalized Debye model.

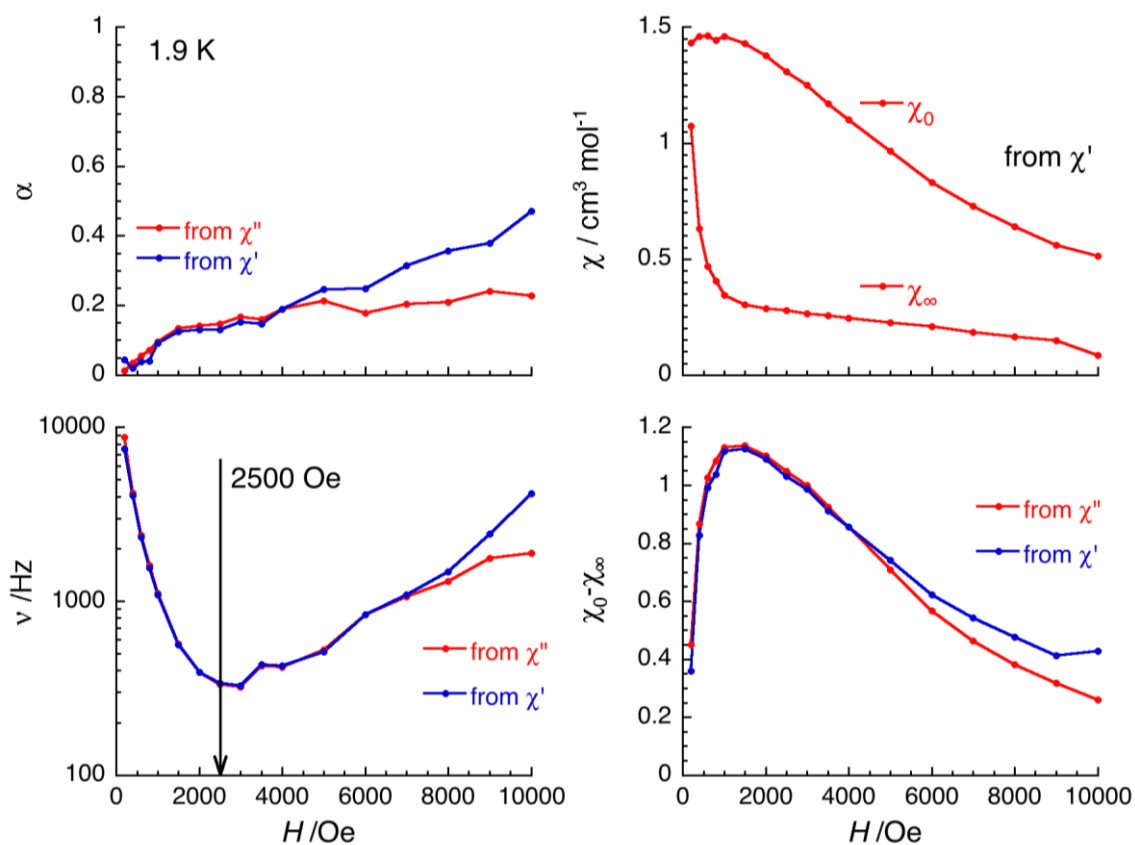


Figure S28. Field dependence of the parameters α , ν , χ_0 , χ_∞ and $\chi_0 - \chi_\infty$ between 0 and 10 kOe deduced from the generalized Debye fit of the frequency dependence of the real (χ') and imaginary (χ'') components of the ac susceptibility at 1.9 K, shown in Figure S27, for **2b**. The slowest relaxation occurs at 2.5 kOe.

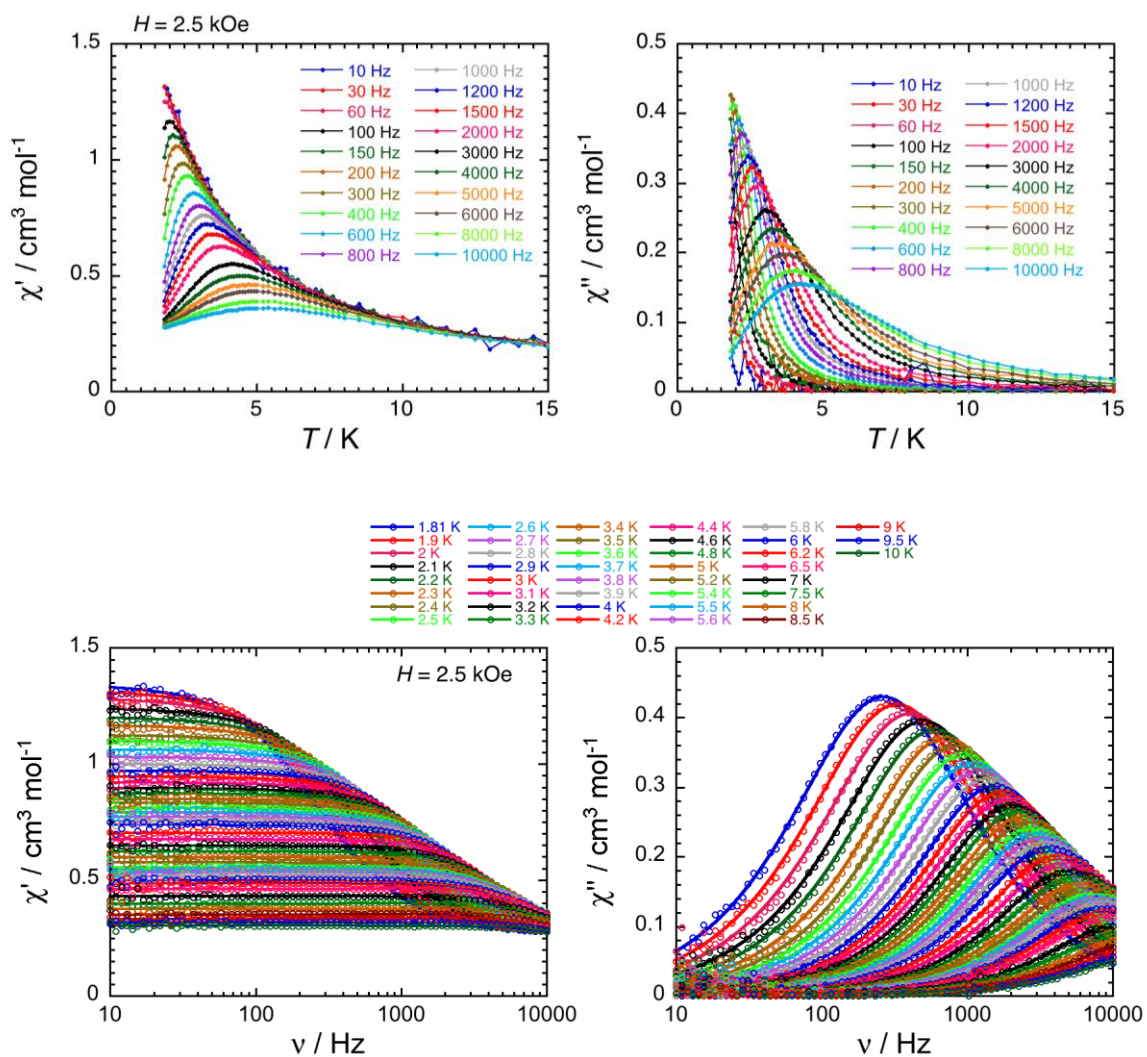


Figure S29. In-phase (left) and out-of-phase (right) components of the molar ac magnetic susceptibility of **2b** measured as a function of temperature at different frequencies (top) and as a function of frequency at different temperatures (bottom) at 2.5 kOe. While solid lines on the top figures are visual guides, the solid curves on the bottom figures provide the best fit using the generalized Debye model.

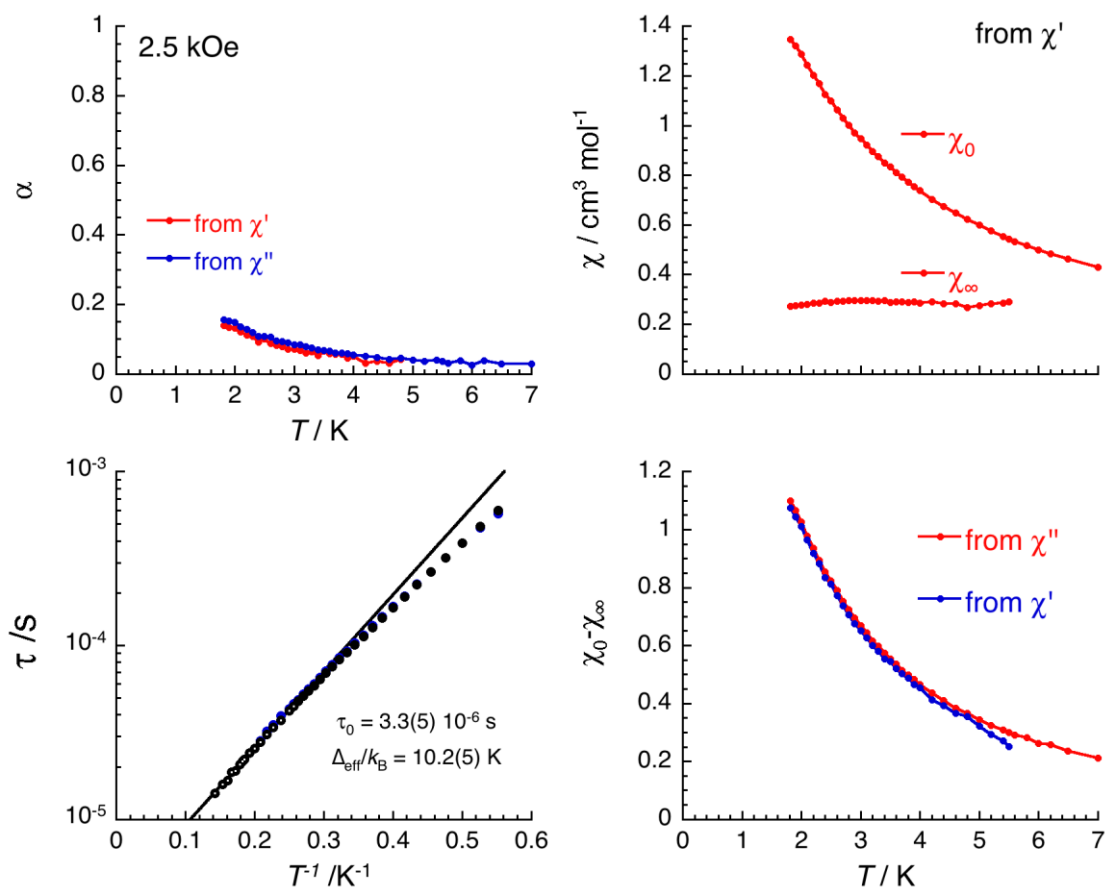


Figure S30. Temperature dependence of the parameters α , τ , χ_0 , χ_∞ and $\chi_0 - \chi_\infty$ between 1.8 and 7 K deduced from the generalized Debye fit of the frequency dependence of the real (χ') and imaginary (χ'') components of the ac susceptibility at 2.5 kOe, shown in Figure S29, for **2b**. On the bottom left figure, the temperature dependence of the relaxation time of **2b** at 2.5 kOe between 1.8 and 7 K (treatment of χ' vs. ν and χ'' vs. ν curves gives indistinguishable results; both sets of data are plotted). The solid line provides the best fit Arrhenius law to the data represented with hollow points with the reported parameter set.

4. EPR spectroscopy

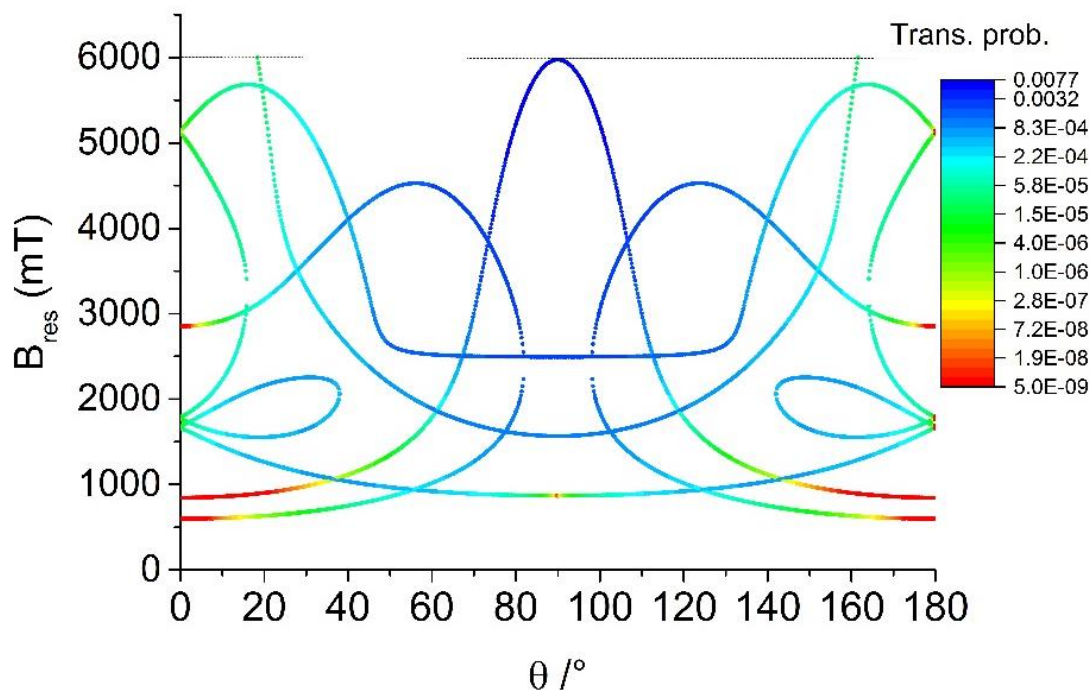


Figure S31. EPR transition roadmap as a function of polar angle θ , calculated for $S = 2$, $D = -1.6 \text{ cm}^{-1}$, $g = 1.99$ and $\nu = 94.27 \text{ GHz}$. Transition probabilities are weighted by relative state population at 6 K.

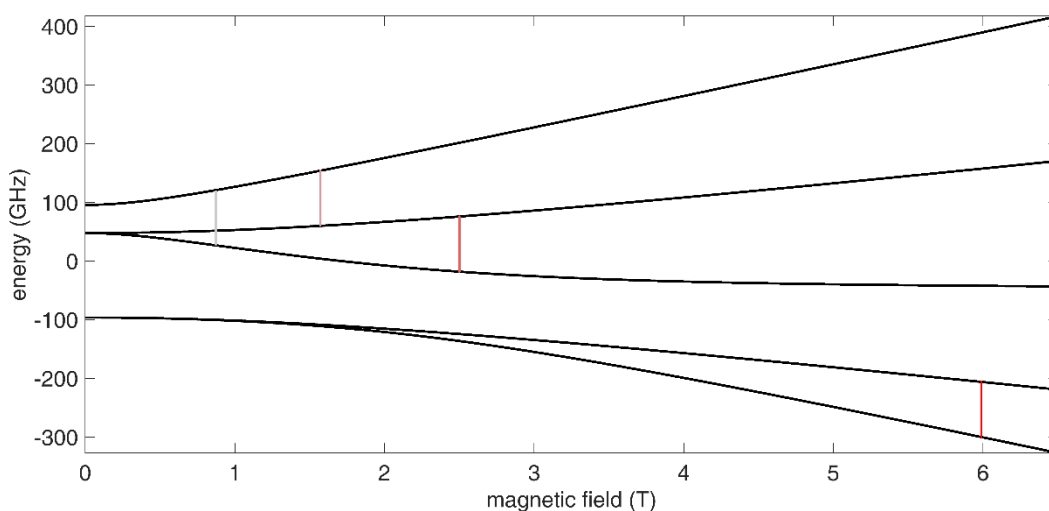


Figure S32. Spin levels calculated for $S = 2$, $D = -1.6 \text{ cm}^{-1}$ and $g = 1.99$ with the magnetic field applied along the X direction. Vertical bars highlight the EPR transitions expected to occur at $\nu = 94.27 \text{ GHz}$. Grey-to-red color scale indicates increasing transition probability.

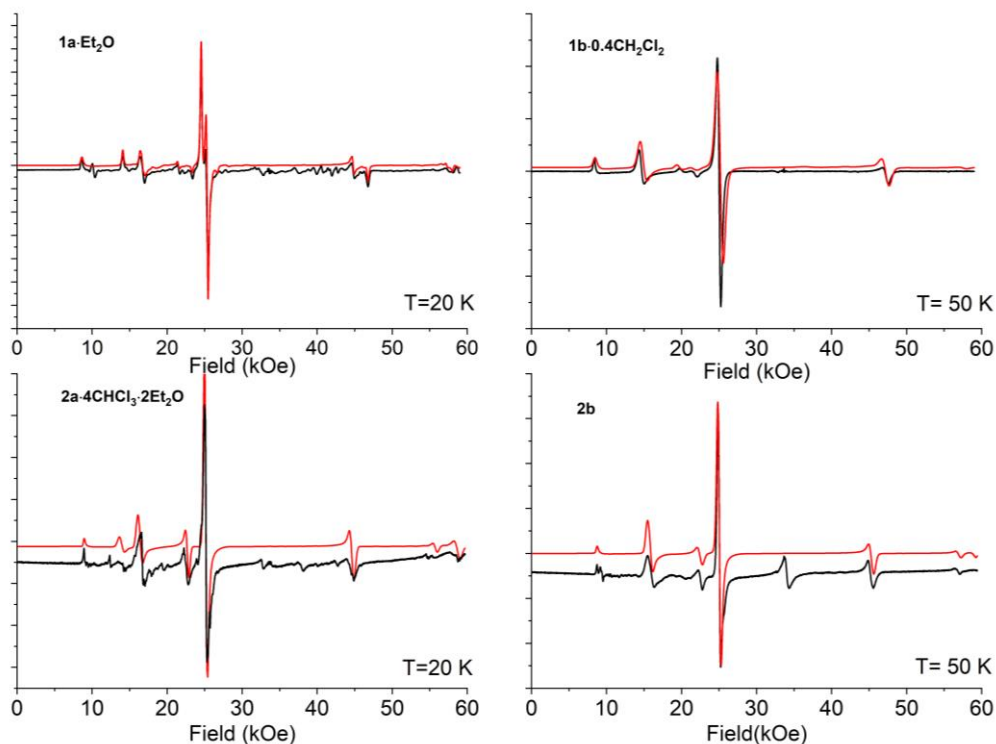


Figure S33. Experimental (black traces) and simulated (red traces) W-band ($\nu = 94.27$ GHz) EPR spectra of polycrystalline samples of the four different compounds recorded at 20 and 50 K.

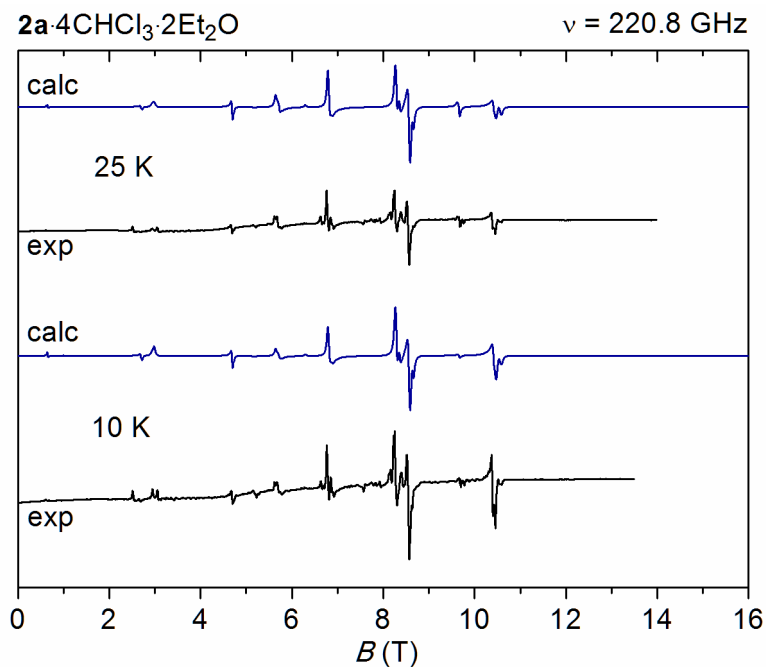


Figure S34. Experimental (black traces) and simulated (blue traces) high-frequency ($\nu = 220.8$ GHz) EPR spectra of **2a-4CHCl₃·2Et₂O** at 10 and 25 K. Simulated spectra were obtained with the parameters indicated in the text, including both the major and the minor species in a 4:1 ratio.

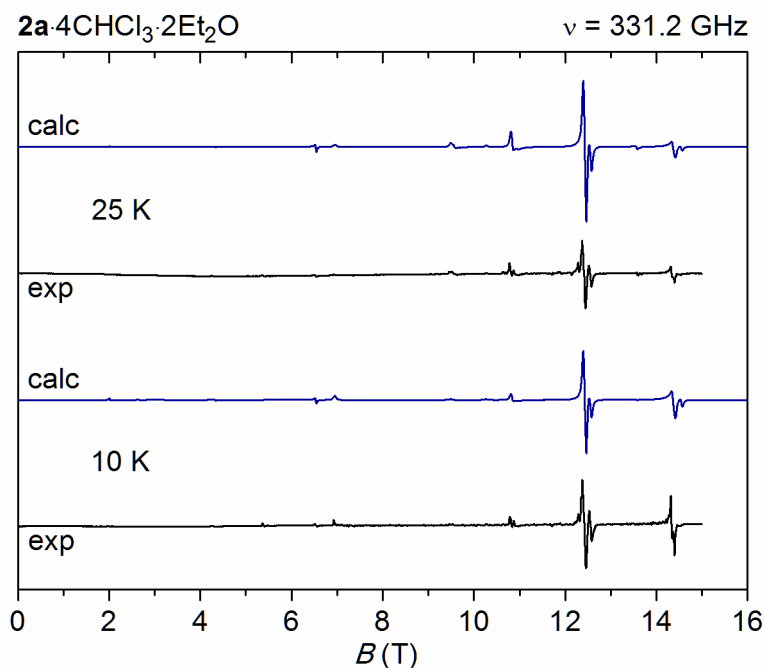


Figure S35. Experimental (black traces) and simulated (blue traces) high-frequency ($\nu = 331.2$ GHz) EPR spectra of **2a**·4CHCl₃·2Et₂O at 10 and 25 K. Simulated spectra were obtained with the parameters indicated in the text, including both the major and the minor species in a 4:1 ratio.

5. *Ab initio* calculations

Evaluation of exchange-coupling constants. The Broken Symmetry (BS) DFT approach was used to calculate the nearest-neighbor and next-nearest-neighbor exchange-coupling constants in **1a**_{sym}. The following determinants were computed: $|+++>$ (**HS**), $|+-+>$ (**BS1**), and $|--+>$ (**BS2**), which is degenerate with $|++->$ (**BS3**) by symmetry. The computed $\langle S^2 \rangle$ values are 42.06, 8.38, and 8.56, respectively. The energies are: -6250.4651573 au (**HS**), -6250.5843150 au (**BS1**), -6250.546828 au (**BS2** and **BS3**). From these values and the spin Hamiltonian $\hat{H} = J_1(\hat{s}_1 \cdot \hat{s}_2 + \hat{s}_2 \cdot \hat{s}_3) + J_2 \hat{s}_1 \cdot \hat{s}_3$, where s_i is the spin vector localized on Cr*i*, exchange-coupling constants are evaluated as $J_1 = 1635$ cm⁻¹ and $J_2 = 606$ cm⁻¹.

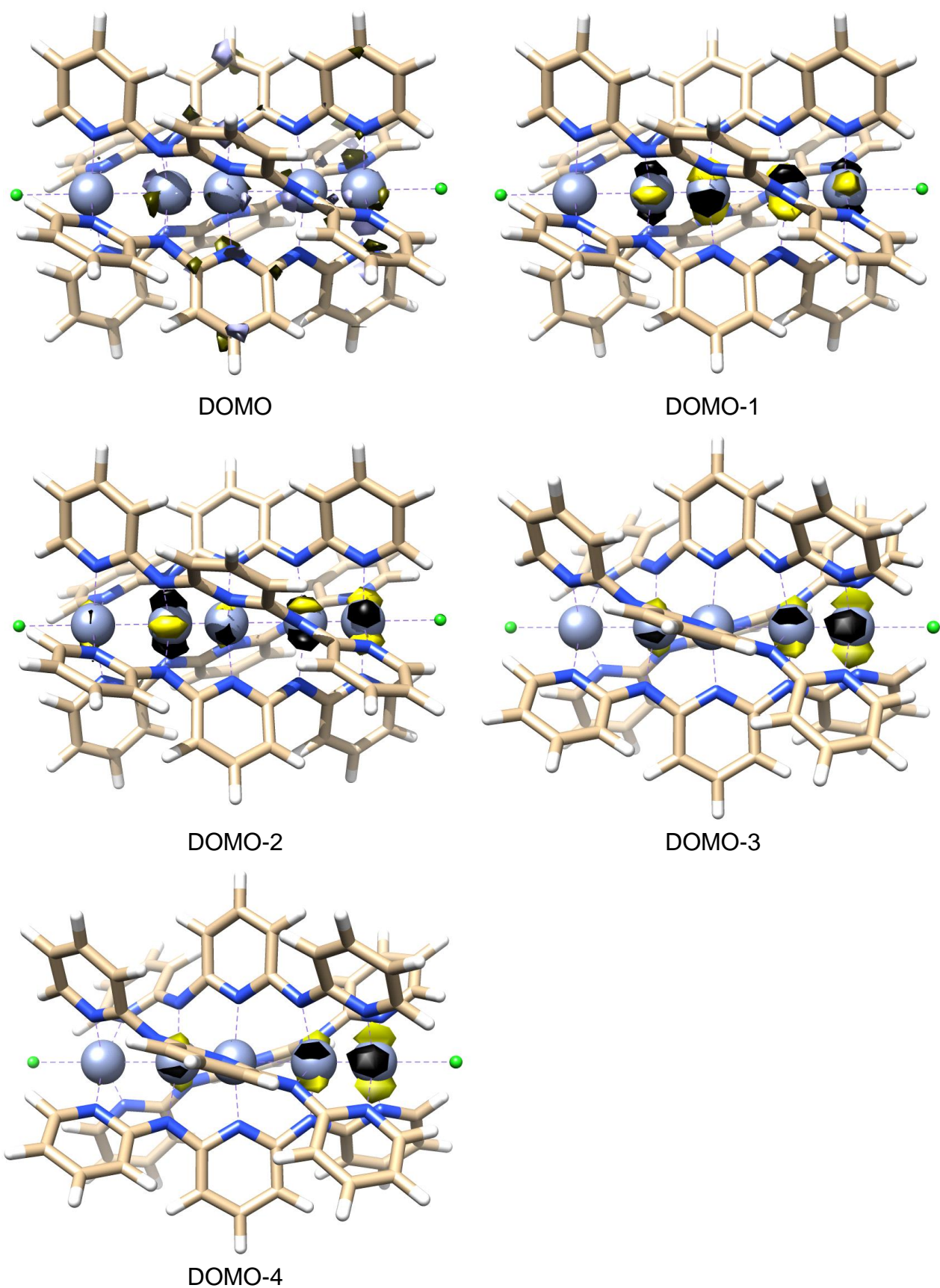


Figure S36. The highest lying DOMOs in $2a_{\text{unsym}}$. Positive and negative signs of the wave function are plotted in yellow and black, respectively.

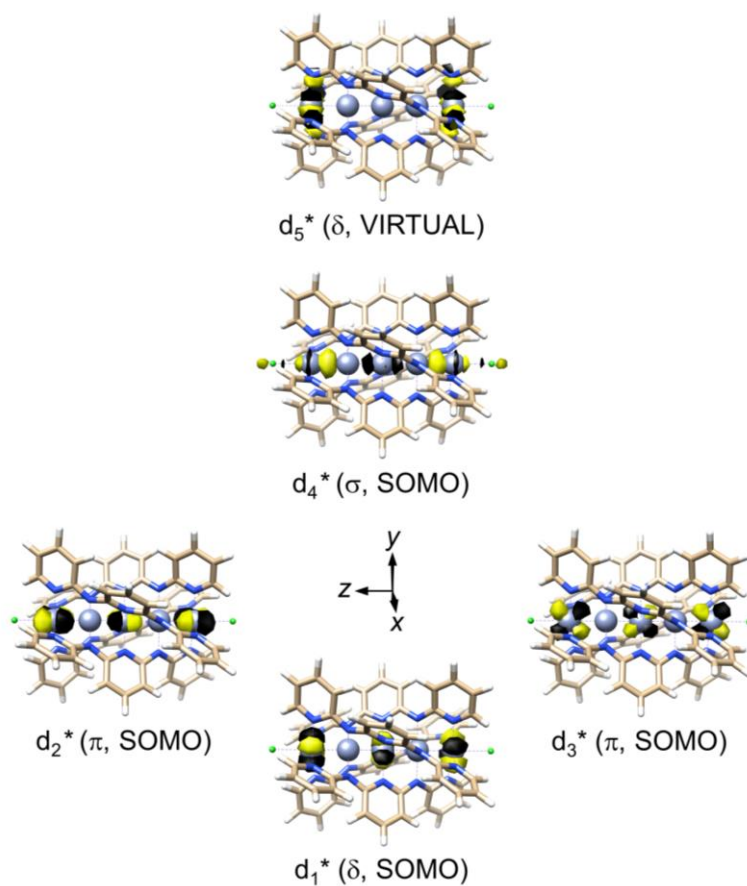


Figure S37. Frontier QROs in $2a_{\text{sym}}$. Positive and negative signs of the wave function are plotted in yellow and black, respectively.

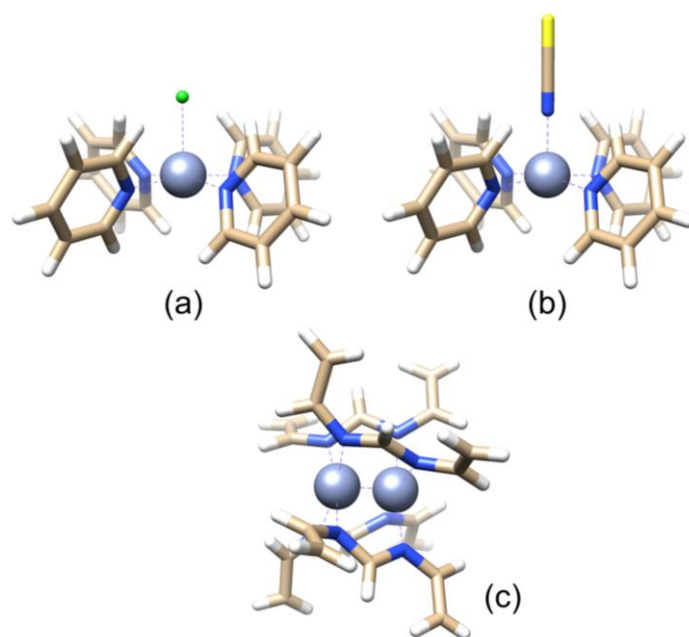


Figure S38. Cr1 model systems for $2a_{\text{unsym}}$ (a) and $2b_{\text{unsym}}$ (b), and Cr2-Cr3 model system for both $2a_{\text{unsym}}$ and $2b_{\text{unsym}}$ (c). The Cr^{2+} ions are represented as silver spheres, while brown, blue, green, yellow, and white colors are used for carbon, nitrogen, chlorine, sulfur, and hydrogen atoms, respectively.

6. Calculation of D parameter using quasi-restricted DFT approach

6.1 Treatment of spin-orbit coupling

Following initial work by Neese et al.,¹⁴⁻¹⁶ spin-orbit (SO) coupling is here represented by the effective one-electron operator:

$$\hat{H}_{\text{SO}} = \sum_i \hat{\mathbf{h}}^{\text{SO}}(i) \cdot \hat{\mathbf{s}}(i) \quad (\text{S1})$$

$$\hat{h}_k^{\text{SO}}(i) = \sum_A \xi(r_{iA}) \hat{l}_k^A(i) \quad (\text{S2})$$

with $k = x, y, z$. In the above equations, i and A sum over electrons and nuclei, respectively, $\hat{\mathbf{s}}(i)$ is the spin operator for the i th electron, $\hat{\mathbf{l}}^A(i)$ is the orbital angular momentum operator for the i th electron relative to the A th nucleus, $\xi(r_{iA})$ is a radial operator, and $r_{iA} = |\mathbf{r}_i - \mathbf{R}_A|$ is the distance between the i th electron (with position vector \mathbf{r}_i) and the A th nucleus (with position vector \mathbf{R}_A). For simplicity, we only include spin-orbit terms involving $A = \text{Cr}^{2+}$ centers.

6.2 Treatment of terminal Cr^{2+} center (Cr1) in pentachromium(II) strings $2\mathbf{a}_{\text{unsym}}$ and $2\mathbf{b}_{\text{unsym}}$

For a complex featuring an isolated Cr^{2+} center (Cr1), Eq. (S2) affords:

$$\hat{h}_k^{\text{SO}}(i) = \xi(r_{i\text{Cr1}}) \hat{l}_k^{\text{Cr1}}(i) \quad (\text{S3})$$

Taking molecular orbitals (MOs), Ψ , to coincide with 3d metal orbitals centered on Cr1, the matrix elements of \hat{h}_k^{SO} can be written as:

$$\langle \Psi' | \hat{h}_k^{\text{SO}} | \Psi \rangle = \zeta_{3\text{d}} \langle \Psi' | \hat{l}_k^{\text{Cr1}} | \Psi \rangle \quad (\text{S4})$$

where the radial integral $\zeta_{3\text{d}}$ is the usual *spin-orbit coupling constant* for a 3d electron of Cr^{2+} (230 cm^{-1} for the free ion).¹⁷ The matrix elements of \hat{l}_k^{Cr1} are available from a number of sources (e.g. Ref.¹⁸) and are gathered in Tables S5-S7 for convenience. Using Eq. (S4) and the spin-resolved orbital energies in Table 8, Eq. (10) of Ref.¹⁵ allows to calculate the contribution of $\alpha \rightarrow \alpha$ (SOMO-VIRTUAL) and $\alpha \rightarrow \beta$ (SOMO-SOMO) excitations to second-order magnetic anisotropy. Notice that the prefactor of $\alpha \rightarrow \beta$ (SOMO-SOMO) term is incorrect in Neese's article, as noted in two subsequent papers.^{19,20} The contributions of these excitations to the diagonal components of the zero-field splitting tensor \mathbf{D} and to the D parameter for the $S = 2$ state (in units of $\zeta_{3\text{d}}^2$) are given by Eqs. (S5a-d) and Eqs. (S6a-d). In these equations as well as in Tables S5-S7, the Cr1 superscript has been dropped for simplicity, but all orbital angular momentum components are relative to Cr1, and all 3d orbitals are centered on Cr1.

$$D_{\alpha \rightarrow \alpha}(zz) = -\frac{1}{4S^2} \frac{|\langle d_{x^2-y^2} | \hat{l}_z | d_{xy} \rangle|^2}{\varepsilon^\alpha(d_{x^2-y^2}) - \varepsilon^\alpha(d_{xy})} = -\frac{1}{4S^2} \frac{4}{\varepsilon^\alpha(d_{x^2-y^2}) - \varepsilon^\alpha(d_{xy})} \quad (\text{S5a})$$

$$D_{\alpha \rightarrow \alpha}(xx) = -\frac{1}{4S^2} \frac{|\langle d_{x^2-y^2} | \hat{l}_x | d_{yz} \rangle|^2}{\varepsilon^\alpha(d_{x^2-y^2}) - \varepsilon^\alpha(d_{yz})} = -\frac{1}{4S^2} \frac{1}{\varepsilon^\alpha(d_{x^2-y^2}) - \varepsilon^\alpha(d_{yz})} \quad (\text{S5b})$$

$$D_{\alpha \rightarrow \alpha}(yy) = -\frac{1}{4S^2} \frac{|\langle d_{x^2-y^2} | \hat{l}_y | d_{xz} \rangle|^2}{\varepsilon^\alpha(d_{x^2-y^2}) - \varepsilon^\alpha(d_{xz})} = -\frac{1}{4S^2} \frac{1}{\varepsilon^\alpha(d_{x^2-y^2}) - \varepsilon^\alpha(d_{xz})} \quad (\text{S5c})$$

$$D_{\alpha \rightarrow \alpha} = D_{\alpha \rightarrow \alpha}(zz) - \frac{1}{2}[D_{\alpha \rightarrow \alpha}(xx) + D_{\alpha \rightarrow \alpha}(yy)] \quad (\text{S5d})$$

$$\begin{aligned} D_{\alpha \rightarrow \beta}(zz) &= \frac{1}{2S(2S-1)} \left\{ \frac{|\langle d_{yz} | \hat{l}_z | d_{xz} \rangle|^2}{\varepsilon^\beta(d_{yz}) - \varepsilon^\alpha(d_{xz})} + \frac{|\langle d_{xz} | \hat{l}_z | d_{yz} \rangle|^2}{\varepsilon^\beta(d_{xz}) - \varepsilon^\alpha(d_{yz})} \right\} = \\ &= \frac{1}{2S(2S-1)} \left\{ \frac{1}{\varepsilon^\beta(d_{yz}) - \varepsilon^\alpha(d_{xz})} + \frac{1}{\varepsilon^\beta(d_{xz}) - \varepsilon^\alpha(d_{yz})} \right\} \end{aligned} \quad (\text{S6a})$$

$$\begin{aligned} D_{\alpha \rightarrow \beta}(xx) &= \frac{1}{2S(2S-1)} \left\{ \frac{|\langle d_{xz} | \hat{l}_x | d_{xy} \rangle|^2}{\varepsilon^\beta(d_{xz}) - \varepsilon^\alpha(d_{xy})} + \frac{|\langle d_{xy} | \hat{l}_x | d_{xz} \rangle|^2}{\varepsilon^\beta(d_{xy}) - \varepsilon^\alpha(d_{xz})} + \frac{|\langle d_{z^2} | \hat{l}_x | d_{yz} \rangle|^2}{\varepsilon^\beta(d_{z^2}) - \varepsilon^\alpha(d_{yz})} + \frac{|\langle d_{yz} | \hat{l}_x | d_{z^2} \rangle|^2}{\varepsilon^\beta(d_{yz}) - \varepsilon^\alpha(d_{z^2})} \right\} = \\ &= \frac{1}{2S(2S-1)} \left\{ \frac{1}{\varepsilon^\beta(d_{xz}) - \varepsilon^\alpha(d_{xy})} + \frac{1}{\varepsilon^\beta(d_{xy}) - \varepsilon^\alpha(d_{xz})} + \frac{3}{\varepsilon^\beta(d_{z^2}) - \varepsilon^\alpha(d_{yz})} + \frac{3}{\varepsilon^\beta(d_{yz}) - \varepsilon^\alpha(d_{z^2})} \right\} \end{aligned} \quad (\text{S6b})$$

$$\begin{aligned} D_{\alpha \rightarrow \beta}(yy) &= \frac{1}{2S(2S-1)} \left\{ \frac{|\langle d_{yz} | \hat{l}_y | d_{xy} \rangle|^2}{\varepsilon^\beta(d_{yz}) - \varepsilon^\alpha(d_{xy})} + \frac{|\langle d_{xy} | \hat{l}_y | d_{yz} \rangle|^2}{\varepsilon^\beta(d_{xy}) - \varepsilon^\alpha(d_{yz})} + \frac{|\langle d_{z^2} | \hat{l}_y | d_{xz} \rangle|^2}{\varepsilon^\beta(d_{z^2}) - \varepsilon^\alpha(d_{xz})} + \frac{|\langle d_{xz} | \hat{l}_y | d_{z^2} \rangle|^2}{\varepsilon^\beta(d_{xz}) - \varepsilon^\alpha(d_{z^2})} \right\} = \\ &= \frac{1}{2S(2S-1)} \left\{ \frac{1}{\varepsilon^\beta(d_{yz}) - \varepsilon^\alpha(d_{xy})} + \frac{1}{\varepsilon^\beta(d_{xy}) - \varepsilon^\alpha(d_{yz})} + \frac{3}{\varepsilon^\beta(d_{z^2}) - \varepsilon^\alpha(d_{xz})} + \frac{3}{\varepsilon^\beta(d_{xz}) - \varepsilon^\alpha(d_{z^2})} \right\} \end{aligned} \quad (\text{S6c})$$

$$D_{\alpha \rightarrow \beta} = D_{\alpha \rightarrow \beta}(zz) - \frac{1}{2}[D_{\alpha \rightarrow \beta}(xx) + D_{\alpha \rightarrow \beta}(yy)] \quad (\text{S6d})$$

6.3 Treatment of trichromium(II) strings $1a_{\text{sym}}$ and $1b_{\text{sym}}$

For a trichromium(II) species, the spatial components of $\hat{\mathbf{h}}^{\text{SO}}(i)$ read as:

$$\hat{h}_k^{\text{SO}}(i) = \xi(r_{i\text{Cr}1}) \hat{l}_k^{\text{Cr}1}(i) + \xi(r_{i\text{Cr}2}) \hat{l}_k^{\text{Cr}2}(i) + \xi(r_{i\text{Cr}3}) \hat{l}_k^{\text{Cr}3}(i) \quad (\text{S7})$$

We introduce the further approximation that spin-orbit terms involving the i th electron and the A th nucleus are only significant when the electron occupies an orbital centered on A (one-electron one-center

approximation).^{21,22} As shown in the main text, the five QROs ($m = 1-5$) herein considered are non-bonding linear combinations of 3d-type orbitals centered on terminal chromium(II) ions ($A = \text{Cr1}, \text{Cr3}$):

$$d_m^* = 2^{-1/2} \left[d_{\Gamma(m)}^{\text{Cr1}} + d_{\Gamma'(m)}^{\text{Cr3}} \right] \quad (\text{S8})$$

where $\Gamma(m)$ and $\Gamma'(m)$ label the particular type of real 3d orbitals involved (xy, xz, yz, z^2, x^2-y^2 , or combinations thereof) expressed in a *local reference frame* with origin on $\text{Cr}j$ ($j = 1, 3$). Since Cr2 does not contribute to these QROs, the second term in Eq. (S7) is irrelevant and the matrix elements between two QROs d_m^* and d_n^* are the sum of two one-center contributions:

$$\langle d_n^* | \hat{h}_k^{\text{SO}} | d_m^* \rangle = 2^{-1} \zeta_{3d} \left[\langle d_{\Gamma(n)}^{\text{Cr1}} | \hat{l}_k^{\text{Cr1}} | d_{\Gamma(m)}^{\text{Cr1}} \rangle + \langle d_{\Gamma'(n)}^{\text{Cr3}} | \hat{l}_k^{\text{Cr3}} | d_{\Gamma'(m)}^{\text{Cr3}} \rangle \right] \quad (\text{S9})$$

To work out the integrals, we express Cr1 - and Cr3 -centered orbitals in two collinear reference frames with origins on Cr1 and Cr3 , respectively. The axes are chosen so as to provide a natural reference frame for Cr1 , with z along Cr1-X and x, y lying on two orthogonal X-Cr1-N planes. In the general case, rotation matrices for real spherical harmonics with $l = 2$ ²³ allow to carry out the required transformation of Cr3 -centered orbitals. In trichromium(II) strings, however, the wave functions can be worked out by simple inspection of Figure 5. The $\text{N-M}\cdots\text{M-N}$ torsion angle defined by the two terminal metals and the N atoms of the same organic ligand amounts to ca. 45° and the basal planes Cr1N_4 and Cr3N_4 are thus twisted by ca. 45° along the chain axis (the same angle is $\sim 90^\circ$ in pentachromium(II) string).

$$B_1 \quad d_1^* = 2^{-1/2} \left(d_{xy}^{\text{Cr1}} - d_{x^2-y^2}^{\text{Cr3}} \right) \quad (\text{S10a})$$

$$E \quad \begin{cases} d_2^* = 2^{-1/2} \left(d_{yz}^{\text{Cr1}} - d_{yz}^{\text{Cr3}} \right) \\ d_3^* = 2^{-1/2} \left(-d_{xz}^{\text{Cr1}} + d_{xz}^{\text{Cr3}} \right) \end{cases} \quad (\text{S10b})$$

$$A_2 \quad d_4^* = 2^{-1/2} \left(-d_{z^2}^{\text{Cr1}} + d_{z^2}^{\text{Cr3}} \right) \quad (\text{S10c})$$

$$B_2 \quad d_5^* = 2^{-1/2} \left(-d_{x^2-y^2}^{\text{Cr1}} - d_{xy}^{\text{Cr3}} \right) \quad (\text{S10d})$$

The attached symmetry labels are based on D_4 molecular symmetry, with the principal fourfold axis Z along the metal chain and the C_2' dyads (X, Y) along the Cr2-N bonds with the amido nitrogens. Group theory predicts that nonzero matrix elements of the Z component of orbital momentum can occur only between d_1^* and d_5^* , or within the (d_2^*, d_3^*) pair; the X, Y components can have nonzero matrix elements between the (d_2^*, d_3^*) pair and d_1^*, d_4^* or d_5^* . The relevant matrix elements can be easily worked out starting from Eqs. (S10a-e) and Tables S5-S7, and are collected in Tables S8-S10. Equations analogous to Eqs. (S5a-c) and (S6a-c) are too cumbersome to be reported here and it is more useful to write them in general form:

$$D_{\alpha \rightarrow \alpha}(kk) = -\frac{1}{4S^2} \sum_{m=1}^4 \frac{|\langle d_5^* | \hat{h}_k^{SO} | d_m^* \rangle|^2}{\varepsilon^\alpha(d_5^*) - \varepsilon^\alpha(d_m^*)} \quad (\text{S11a})$$

$$D_{\alpha \rightarrow \beta}(kk) = \frac{1}{2S(2S-1)} \sum_{m,n=1}^4 \frac{|\langle d_n^* | \hat{h}_k^{SO} | d_m^* \rangle|^2}{\varepsilon^\beta(d_n^*) - \varepsilon^\alpha(d_m^*)} \quad (n \neq m) \quad (\text{S11b})$$

where the required matrix elements and spin-resolved orbital energies are given in Tables S8-S10 and 8.

Table S5. On-site matrix elements $\langle \Psi' | \hat{l}_z | \Psi \rangle$ between 3d orbitals relevant for single-particle $\alpha \rightarrow \alpha$ and $\alpha \rightarrow \beta$ spin excitations from Ψ to Ψ' . Elements in blue do not enter calculations and are only given for completeness.

$\Psi' \setminus \Psi$	d_{xy}	d_{xz}	d_{yz}	d_{z^2}	$d_{x^2-y^2}$
d_{xy}					$2i$
d_{xz}			$-i$		
d_{yz}		i			
d_{z^2}					
$d_{x^2-y^2}$	$-2i$				

Table S6. On-site matrix elements $\langle \Psi' | \hat{l}_z | \Psi \rangle$ between 3d orbitals relevant for single-particle $\alpha \rightarrow \alpha$ and $\alpha \rightarrow \beta$ spin excitations from Ψ to Ψ' . Elements in blue do not enter calculations and are only given for completeness.

$\Psi' \setminus \Psi$	d_{xy}	d_{xz}	d_{yz}	d_{z^2}	$d_{x^2-y^2}$
d_{xy}		$-i$			
d_{xz}	i				
d_{yz}				$-i\sqrt{3}$	$-i$
d_{z^2}			$i\sqrt{3}$		
$d_{x^2-y^2}$			i		

Table S7. On-site matrix elements $\langle \Psi' | \hat{l}_y | \Psi \rangle$ between 3d orbitals relevant for single-particle $\alpha \rightarrow \alpha$ and $\alpha \rightarrow \beta$ spin excitations from Ψ to Ψ' . Elements in blue do not enter calculations and are only given for completeness.

$\Psi' \setminus \Psi$	d_{xy}	d_{xz}	d_{yz}	d_{z^2}	$d_{x^2-y^2}$
d_{xy}			i		
d_{xz}				$i\sqrt{3}$	$-i$
d_{yz}	$-i$				
d_{z^2}		$-i\sqrt{3}$			
$d_{x^2-y^2}$		i			

Table S8. Matrix elements $\langle d_n^* | \hat{h}_z^{SO} | d_m^* \rangle$ (in units of ζ_{3d}) relevant for single-particle $\alpha \rightarrow \alpha$ and $\alpha \rightarrow \beta$ spin excitations from d_m^* to d_n^* . Elements in blue do not enter calculations and are only given for completeness.

$d_n^* \setminus d_m^*$	d_1^*	d_2^*	d_3^*	d_4^*	d_5^*
d_1^*					$-2i$
d_2^*			$-i$		
d_3^*		i			
d_4^*					
d_5^*	$2i$				

Table S9. Matrix elements $\langle d_n^* | \hat{h}_x^{SO} | d_m^* \rangle$ (in units of ζ_{3d}) relevant for single-particle $\alpha \rightarrow \alpha$ and $\alpha \rightarrow \beta$ spin excitations from d_m^* to d_n^* . Elements in blue do not enter calculations and are only given for completeness.

$d_n^* \setminus d_m^*$	d_1^*	d_2^*	d_3^*	d_4^*	d_5^*
d_1^*		$i/2$	$i/2$		
d_2^*	$-i/2$			$i\sqrt{3}$	$i/2$
d_3^*	$-i/2$				$-i/2$
d_4^*		$-i\sqrt{3}$			
d_5^*		$-i/2$	$i/2$		

Table S10. Matrix elements $\langle d_n^* | \hat{h}_y^{SO} | d_m^* \rangle$ (in units of ζ_{3d}) relevant for single-particle $\alpha \rightarrow \alpha$ and $\alpha \rightarrow \beta$ spin excitations from d_m^* to d_n^* . Elements in blue do not enter calculations and are only given for completeness.

$d_n^* \setminus d_m^*$	d_1^*	d_2^*	d_3^*	d_4^*	d_5^*
d_1^*		$i/2$	$-i/2$		
d_2^*	$-i/2$				$-i/2$
d_3^*	$i/2$			$i\sqrt{3}$	$-i/2$
d_4^*			$-i\sqrt{3}$		
d_5^*		$i/2$	$i/2$		

7. References

- (1) Armarego, W. L. F. *Purification of laboratory chemicals*, 5th ed.; Elsevier, Ed.; Butterworth-Heinemann: Burlington, United States, 2003.
- (2) Yang, M.; Lin, T.-W.; Chou, C.-C.; Lee, H.-C.; Chang, H.-C.; Lee, G.-H.; Leung, M.; Peng, S.-M. New oligo- α -pyridylamino ligands and their metal complexes. *Chem. Commun.* **1997**, No. 23, 2279–2280.
- (3) Wang, C.; Lo, W.; Chou, C.; Lee, G.; Chen, J.; Peng, S. Synthesis, Crystal Structures, and Magnetic Properties of a Series of Linear Pentanickel(II) Complexes: $[\text{Ni}_5(\mu_5\text{-tpda})_4\text{X}_2]$ ($\text{X} = \text{Cl}^-$, CN^- , N_3^- , NCS^-) and $[\text{Ni}_5(\mu_5\text{-tpda})_4(\text{CH}_3\text{CN})_2](\text{PF}_6)_2$ (tpda^{2-} = the tripyridyldiamido dianion). *Inorg. Chem.* **1998**, 37 (16), 4059–4065.
- (4) Clérac, R.; Cotton, F. A.; Daniels, L. M.; Dunbar, K. R.; Murillo, C. A.; Pascual, I. Linear Trichromium Complexes with Direct Cr to Cr Contacts. 1. Compounds with $\text{Cr}_3(\text{dipyridylamide})_4^{2+}$ Cores. *Inorg. Chem.* **2000**, 39 (4), 748–751.

- (5) Berry, J. F.; Cotton, F. A.; Murillo, C. A.; Chan, Z.-K.; Yeh, C.-W.; Chen, J.-D. Linear Trichromium, Tricobalt, Trinickel, and Tricopper Complexes of 2,2'-Dipyridylamide. *Inorg. Syn.* **2014**, *36*, 103–110.
- (6) Berry, J. F.; Cotton, F. A.; Lu, T.; Murillo, C. A.; Roberts, B. K.; Wang, X. Molecular and electronic structures by design: Tuning symmetrical and unsymmetrical linear trichromium chains. *J. Am. Chem. Soc.* **2004**, *126* (22), 7082–7096.
- (7) Wu, L.-C.; Thomsen, M. K.; Madsen, S. R.; Schmoekel, M.; Jørgensen, M. R. V.; Cheng, M.-C.; Peng, S.-M.; Chen, Y.-S.; Overgaard, J.; Iversen, B. B. Chemical Bonding in a Linear Chromium Metal String Complex. *Inorg. Chem.* **2014**, *53* (23), 12489–12498.
- (8) Chang, H.; Li, J.; Wang, C.; Lin, T.; Lee, H.-C.; Lee, G.; Peng, S. Linear Five-Centred Chromium Multiple Bonds Bridged by Four tpd²⁻ Ligands [tpd²⁻ = tripyridyldiamido dianion] – Synthesis and Structural Studies. *Eur. J. Inorg. Chem.* **1999**, *1999* (8), 1243–1251.
- (9) Ismayilov, R. H.; Wang, W.-Z.; Lee, G.-H.; Chien, C.-H.; Jiang, C.-H.; Chiu, C.-L.; Yeh, C.-Y.; Peng, S.-M. Redox Modification of EMACs Through the Tuning of Ligands: Heptametal(II) Complexes of Pyrazine-Modulated Oligo- α -pyridylamido Ligands. *Eur. J. Inorg. Chem.* **2009**, *2009* (14), 2110–2120.
- (10) M. Llunell, D. Casanova, J. Cirera, P. Alemany, S. A. *SHAPE v2.1 - Continuous Shape Measures calculation*; Universitat de Barcelona, Spain, 2013.
- (11) Cotton, F. A.; Daniels, L. M.; Murillo, C. A.; Wang, X. Getting the right answer to a key question concerning molecular wires. *Chem. Commun.* **1999**, *5* (24), 2461–2462.
- (12) *E04FCF, E04YCF and F02ABF, NAG Fortran Library Routines (Mark 17)*; NAG Ltd: Oxford, UK, 1996.
- (13) Chumakova, N. A.; Yankova, T. S.; Vorobiev, A. K. EPR Study of the Orientation Distribution Function of HO₂• Radicals Ordered by Light Irradiation. *Appl. Magn. Reson.* **2008**, *33* (1–2), 117–126.
- (14) Neese, F.; Solomon, E. I. Calculation of Zero-Field Splittings, g-Values, and the Relativistic Nephelauxetic Effect in Transition Metal Complexes. Application to High-Spin Ferric Complexes. *Inorg. Chem.* **1998**, *37* (26), 6568–6582.
- (15) Neese, F. Importance of Direct Spin–Spin Coupling and Spin-Flip Excitations for the Zero-Field Splittings of Transition Metal Complexes: A Case Study. *J. Am. Chem. Soc.* **2006**, *128* (31), 10213–10222.
- (16) Neese, F. Calculation of the zero-field splitting tensor on the basis of hybrid density functional and Hartree-Fock theory. *J. Chem. Phys.* **2007**, *127* (16), 164112.
- (17) Griffith, J. S. *The Theory of Transition-Metal Ions*; Cambridge University Press: London, 1961.
- (18) Kahn, O. *Molecular Magnetism*; VCH-Verlag: Weinheim, 1993.
- (19) Schmitt, S.; Jost, P.; van Wüllen, C. Zero-field splittings from density functional calculations: Analysis and improvement of known methods. *J. Chem. Phys.* **2011**, *134* (19), 194113.
- (20) Sugisaki, K.; Toyota, K.; Sato, K.; Shiomi, D.; Takui, T. Quasi-Restricted Orbital Treatment for the Density Functional Theory Calculations of the Spin–Orbit Term of Zero-Field Splitting Tensors. *J. Phys. Chem. A* **2016**, *120* (49), 9857–9866.

- (21) Cohen, J. S.; Wadt, W. R.; Hay, P. J. Spin-orbit coupling and inelastic transitions in collisions of O(1D) with Ar, Kr, and Xe. *J. Chem. Phys.* **1979**, *71* (7), 2955–2965.
- (22) Marian, C. M. Spin-Orbit Coupling in Molecules. In *Reviews in Computational Chemistry, Vol. 17*; Lipkowitz, K. B., Boyd, D. B., Eds.; John Wiley & Sons, Inc.: New York, 2001; pp 99–204.
- (23) Ivanic, J.; Ruedenberg, K. Rotation Matrices for Real Spherical Harmonics. Direct Determination by Recursion. *J. Phys. Chem.* **1996**, *100* (15), 6342–6347.